https://doi.org/10.5194/egusphere-2026-3027
Preprint. Discussion started: 16 June 2026

Coarse-mode sea spray aerosols enhance warm rain formation in in marine low clouds.

Katherine Mifsud[1], Jason Barr[1], Robert Wood[1], Yonghoon Choi[2,3], Ewan Crosbie[2,3], Glenn S. Diskin[2], Joshua P. DiGangi[2], Richard H. Moore[2], Claire Robinson[2+], Michael A. Shook[2], Armin Sorooshian[4,5], Christiane Voigt[6,7], Luke Ziemba[2]

[1]Department of Atmosphere and Climate Sciences, University of Washington, Seattle, 98195, USA
[2]NASA Langley Research Center, Hampton, VA, 23681, USA
[3]Analytical Mechanics Associates, Hampton, VA 23666, USA
[4]Department of Chemical and Environmental Engineering, University of Arizona, Tucson, AZ, 85721, USA
[5]Department of Hydrology and Atmospheric Sciences, University of Arizona, Tucson, AZ, 85721, USA
[6]Institute of Atmospheric Physics, German Aerospace Center (DLR), 82234 Wessling, Germany
[7]Institute of Atmospheric Physics, Johannes Gutenberg University Mainz, 55099 Mainz, Germany
[+]Deceased

Correspondence to: Katherine Mifsud (kathem24@uw.edu)

Abstract. Precipitation in low clouds affects cloud responses to aerosol perturbations, thereby impacting aerosol radiative forcing of climate, a significant but indeterminate contribution to uncertainty in future warming. The onset of drizzle formation in marine low clouds may be influenced by the presence of supermicron sea salt aerosols. These particles can act as giant CCN (GCCN) that benefit from rapid condensational growth to a size that initiates collision-coalescence. Aircraft-based in-situ observations of cloud microphysical properties and aerosol size distributions from the Aerosol Cloud meTeorology Interactions oVer the western ATlantic Experiment (ACTIVATE) are analyzed from January-June 2022. Observations from a cloud aerosol spectrometer and a cloud droplet probe in clear air are used to quantify GCCN size distributions. Modest correlations are found between GCCN and near surface-level wind speeds when averaged together into wind speed bins, a result consistent with other studies. Observed GCCN distributions and cloud thicknesses are used to drive simulations within a 1-dimensional kinematic super droplet model, exploring the conditions under which the observed GCCN distributions induce a first-order impact on precipitation rate. The model demonstrates that even relatively small GCCN salt masses (~1 μg m^{-3}) can accelerate the onset of drizzle in lightly precipitating marine low clouds. Similarly, a statistical analysis of in-cloud data shows the ratio of rainwater to total condensed water is higher when GCCN concentration/mass is above average. Together, the results indicate a significant influence of GCCN on precipitation formation in marine low clouds.

1 Introduction

Cloud-aerosol interactions have a significant impact on climate, particularly through their influence on marine stratocumulus clouds, which cover roughly 20% of the planet's oceans and play a dominant role in modulating Earth's radiative energy balance (Hartmann and Short 1980). These interactions affect both cloud microphysics and macrophysics, including cloud albedo and lifetime, thereby altering the reflection of solar radiation and the overall radiative forcing of the climate system (Seinfeld et al., 2016). By regulating heat, moisture, and momentum exchanges between the ocean and atmosphere, the stratocumulus-topped boundary layer (STBL) profoundly influences large-scale climate systems (Wood 2012). Marine stratocumuli reflect a large portion of the Earth's incoming solar radiation,

https://doi.org/10.5194/egusphere-2026-3027
Preprint. Discussion started: 16 June 2026

while only minimally contributing to outgoing longwave radiation (Chen et al., 2000). This combination of radiative effects and expansive coverage makes stratocumulus clouds integral to the planet's overall radiative budget (Stephens and Greenwald 1991; Hartmann et al. 1992; Wood 2012; L'Ecuyer et al., 2019). Unfortunately, clouds are the largest uncertainty in estimates and interpretations of the Earth's rapidly changing energy budget, and much of the uncertainty revolves around how aerosols interact with stratocumulus clouds (Pachauri et al., 2014, Bellouin et al., 2020; von Salzen et al., 2025). The Twomey effect (Twomey, 1977) describes how increases in cloud droplet concentration resulting from aerosol-cloud interactions (ACI) reduce droplet size and increase total droplet surface area for a fixed amount of condensate. As a result, clouds reflect more solar radiation, even without changes in cloud liquid water content. However, changes in droplet size can also drive adjustments to cloud macrophysical properties by changing precipitation and cloud top entrainment rate (Ackerman et al., 2004; Wood 2007; Bellouin et al., 2020). These precipitation and droplet sedimentation processes, which impact how cloud condensate and cover adjust in response to aerosol changes, remain challenging to quantify making them a persistent source of uncertainty in climate models (Stevens and Feingold, 2009). As these interactions occur on sub-kilometer scales, Earth system models poorly represent these cloud adjustments (e.g., Mülmenstädt and Feingold 2018). Cloud condensation nuclei (CCN) play a crucial role in aerosol-cloud-precipitation processes, by increasing cloud droplet concentration, which reduces cloud droplet size for a given amount of condensate, thereby decreasing precipitation efficiency (Albrecht 1989; Beard and Ochs 1993; Pawlowska et al., 2003; Terai et al., 2012; Mann et al., 2014). The ability of a cloud system to create a few large droplets (~15-20 μm radius) greatly influences its capacity to generate precipitation through collision-coalescence (Hocking 1959; Berry 1967; Albrecht et al., 1989; Wood et al., 2009). There are two pathways to forming large droplets. First, reducing the overall number of CCN will result in each cloud droplet being bigger (for a given condensate amount), and then collision-coalescence may be able to grow a few lucky drops that end up accelerating the collision-coalescence. Second, if present in sufficient amounts, giant CCN can also grow efficiently by condensation to radii of 15-20 micron.

1.1 Giant cloud condensation nuclei

Drizzle formation can be achieved through the existence of a tail of large "collector" droplets formed on giant cloud condensation nuclei (GCCN) that can initiate collision-coalescence (Ludlam 1951; Johnson 1982; Feingold et al., 1999; Jensen and Lee 2008, Jensen and Nugent 2017; Dziekan et al., 2021). In marine environments giant sea spray particles with dry diameters larger than ~2 μm enhances collision-coalescence, in contrast to smaller particles that suppress it. Based on this finding, we define GCCN as salt particles with dry diameters larger than 2 μm. Condensational growth of GCCN from the ocean surface through the cloud is important for growing the particles to a size where they can initiate collision-coalescence (Ludlam 1951; Jensen and Nugent 2017). Despite a solid theoretical foundation, this effect has not yet been incorporated into physical parameterizations used in bulk microphysical models, which may lead to an underestimation of warm rain formation in some clouds (Jensen and Nugent 2017; Dziekan et al., 2021). Cloud droplets grown on GCCN are highly concentrated solutions compared with the majority of cloud droplets, which are grown on much smaller accumulation mode aerosol particles (with typical dry diameters of ~0.1 μm). This accelerates, via the Raoult effect (Jensen and Nugent 2017), the condensational growth rates of

https://doi.org/10.5194/egusphere-2026-3027
Preprint. Discussion started: 16 June 2026

droplets grown on GCCN compared with those forming on accumulation mode CCN. In some cases, this may lead to a faster onset of warm rain (L'Ecuyer et al., 2009). The fundamental challenge to representing GCCN in microphysical models is that the condensational growth rate of cloud droplets depends not only on their size but also on the mass of salt they contain. GCCN-containing droplets must therefore be treated as a distinct category of cloud hydrometeor, increasing model complexity. Posselt and Lohmann (2008) attempted to incorporate GCCN effects into a global climate model by parameterizing GCCN by assuming they directly activate into raindrops; however, this approach neglects detailed condensational growth processes. It is computationally-challenging to accurately capture this aerosol-dependent condensational growth in microphysical models, but it can be achieved using super droplet methods (Shima et al., 2009; Shima et al., 2020; Li at al., 2022; Zmijewski et al., 2024), or by using two-dimensional bin microphysical schemes that independently keep track of hydrometeor wet sizes as well as the aerosol dry size (e.g., Flossman 1985; Lebo and Morrison 2013). Since droplets formed on GCCN remain highly concentrated salt solutions, they can more easily resist evaporation and the larger GCCN can even continue growing by condensation as they descend through (weakly) subsaturated downdrafts (Jensen and Nugent 2017). This contrasts with smaller cloud droplets grown on accumulation mode aerosol, which typically lose mass and may completely evaporate in similar conditions.

Despite advances in understanding GCCN's role in collision-coalescence growth, significant uncertainties remain due to wide variations in the sizes and concentrations reported in prior studies. For example, Jensen and Nugent (2017) found that introducing 1 μm dry radius GCCN at concentrations of 0.3 cm^{-3} could influence drizzle in a microphysical parcel model, while Feingold et al. (1999) introduced 20 μm droplets, a proxy for condensationally-grown GCCN, into large eddy simulations at concentrations as low as 10^{-4} to 10^{-2} cm^{-3} and found impacts on precipitation for the higher concentrations. Because condensational growth of GCCN was not treated explicitly in Feingold et al. (1999), it is difficult to compare this result with other studies, highlighting major differences in model assumptions and methods. Lowenstein et al. (2010) used aerosol and cloud probe observations of hydrated giant haze particles below marine trade cumulus to initialize a parcel model that produced a tail of large droplets (r~20-100 μm) above cloud base that matched observations fairly on two flight days. However, model simulations were not conducted without GCCN, so the overall impact of the GCCN is unclear.

Dziekan et al. (2021) have performed the most sophisticated and realistic simulations of GCCN influences on low cloud precipitation to date, using a super droplet model embedded within a large eddy model. The model explicitly computes both the condensational and coalescence growth of GCCN, and shows that GCCN from an observed flight over the southeastern Pacific is sufficient to increase cloud base precipitation rate in a marine stratocumulus cloud case by ~50% compared with the case with zero GCCN. A somewhat weaker influence (~10%) was found in a deeper trade cumulus case. The base LES case used in Dziekan et al. (2021) used observed GCCN measurements with near-surface GCCN dry salt mass of ~6 $\mu g\ m^{-3}$ and number concentration of ~0.22 cm^{-3} (for dry diameters exceeding 2 μm) with a near-surface wind speed of 5.4 $m\ s^{-1}$. Sensitivity tests were conducted for larger GCCN concentrations/masses

https://doi.org/10.5194/egusphere-2026-3027
Preprint. Discussion started: 16 June 2026

to show that further increasing GCCN loading continued to increase precipitation rate, with a factor of 5 increase leading to precipitation rate increases of ~300% (stratocumulus) and ~30% (cumulus) above the rate without GCCN.

GCCN dry size distributions in previous studies are typically found to decrease approximately exponentially with increasing particle diameter (e.g., Woodcock, 1953; Lewis and Schwartz, 2004; Cólon-Robles et al., 2006). Because the observed e-folding diameter for the decrease is relatively small (see section 2.2 below), this means that reported GCCN number concentrations are particularly sensitive to the threshold dry diameter D_{min} used to define GCCN. Although several recent studies have adopted a threshold D_{min}~2 μm, studies do not always report what threshold diameter was used or use a hydrated size threshold rather than a dry one (e.g., Colón-Robles et al., 2006), making cross-study comparisons of observed GCCN and their influences on clouds challenging (Cooper et al., 2013).

This work aims to address critical gaps in understanding coarse-mode cloud-aerosol interactions in marine low clouds. We utilize a robust observational framework, which includes a very large number of flight legs across different seasons and meteorological conditions, established by the NASA Earth Venture Sub-Orbital (EVS-3) Aerosol Cloud meTeorology Interactions oVer the western ATlantic Experiment (ACTIVATE) field campaign. Building on previous work (e.g., Woodcock, 1953; Colón-Robles et al., 2006), we first document coarse-mode aerosol size distributions under clear sky conditions below cloud for a wide variety of aircraft flights and examine how near-surface wind speed influences their number and mass concentration and size distribution. We then investigate the extent to which our observed variations in GCCN concentrations can modulate precipitation in marine stratocumulus clouds using a super droplet model. The goal is to determine how each of the observed GCCN distributions alters the cloud droplet size distribution and accelerates precipitation formation under varying aerosol conditions and for a range of plausible macrophysical and microscale turbulence conditions. We also examine the influence of GCCN on observationally derived rainwater content (RWC), calculated from ACTIVATE observations, which provides a purely observational perspective on GCCN-precipitation relationships. Together, the modeling and observation analyses provide a comprehensive understanding of how GCCN impact warm rain formation. This analysis is necessary not only to improve our understanding of aerosol-cloud interactions, but also to contribute to better parameterizations that include the impact of GCCN.

2 Methods

2.1 Dataset

ACTIVATE is a NASA Sub-Orbital field campaign that flew aircraft and captured data from February 2020 through June 2022 with the intent of providing globally important data detailing changes in warming and cooling planetary feedbacks, atmospheric aerosols and sources, and marine boundary layer cloud systems (Sorooshian et al., 2023). The observations relevant to this study were collected during two deployments spanning January to June 2022 to capture different seasonal states and broaden the range of aerosol and meteorological conditions. Flights were conducted using a twin-aircraft design based out of NASA Langley Research Center in Virginia, with the HU-25 Falcon flying at lower

https://doi.org/10.5194/egusphere-2026-3027
Preprint. Discussion started: 16 June 2026

altitudes (0.15 to 3 km) and the King Air flying above (8 to 10 km). In this study, only data from the low-flying Falcon are used. We utilize measurements taken from the Diode Laser Hygrometer (DLH) which measures relative humidity, Cloud Droplet Probe (CDP), Cloud-Aerosol Spectrometer (CAS), and the two-dimensional Stereo Probe (2D-S), all of which were externally mounted on the Falcon. The CAS measures from 0.5 μm diameter to 50 μm diameter and the CDP measures from 2 μm to 50 μm diameter. Both probes measure cloud droplet size distributions, from which aerosol and cloud droplet number concentration, liquid water content, effective radius, and effective variance are derived (Baumgardner 2001; Lance 2012). The 2D-S measures larger drop number size distribution for liquid and ice both separately and combined; liquid water content; effective diameter and median volume diameter (Kirschler et al., 2023). The 2D-S also measures a broader size range from 29 to 1465 μm diameter. While a Fast Cloud Droplet Probe (FCDP) was available during the campaign, it is not included in this analysis. The FCDP lower diameter threshold is 3 μm diameter, so it doesn't quite reach the 2 μm diameter threshold we were looking for. This study focuses on in-situ Falcon data collected between 150 m and 2.5 km altitude. A total of 75 joint flights on 43 days, logging upwards of 120 flight hours were conducted during the 2022 deployment, making it the most comprehensive year due to fewer pandemic disruptions compared to 2020–2021 (Sorooshian et al., 2023).

We focus on Falcon flight legs classified as BCB (below cloud base) to analyze coarse-mode aerosols (section 2.2-3.2), and ACB (above cloud base) and BCT (below cloud top) when working in-cloud (section 3.3). These legs are a part of "cloudy ensembles", which are sequences of flight legs conducted in close succession that sample different vertical regions of the cloud and sub-cloud environment, where leg is about 3 minutes long (Sorooshian et al., 2023). The vast majority of available data come from cloudy ensembles, which account for over 90% of the total flight legs in 2022. We did not utilize flight legs from designated "clear-sky" ensembles due to insufficient data (see Sorooshian et al., 2023). Less than 10% of the total ensembles in 2022 are "clear-sky." The systematic repetition of these flight ensembles has resulted in an extensive and structured dataset (Dadashazar et al., 2022; Sorooshian et al., 2023). However, we aim to use BCB legs without cloud contamination, so to filter for clear sky conditions, we apply a liquid water content threshold of 0.0025 g m^{-3} from the CAS and the CDP and remove data points above this threshold to remove contamination from cloud droplets. We further restrict the dataset by requiring that the precipitation number concentration, defined as the concentration of precipitation-sized particles measured by the 2D-S probe, remains below 100 m^{-3}. This additional criterion ensures that drizzle-sized drops are not present. We also remove data points with relative humidity (RH) above 95%, given that there is a ~5% error in RH measurements, to further ensure that the sampled air is subsaturated. Together, these thresholds ensure that the observed hydrated size distributions are indeed characterizing haze droplets in subsaturated conditions without cloud or drizzle droplet interference.

2.2 Constructing dry size distributions

To characterize aerosol concentration above the Western Atlantic, we analyze size-resolved hydrated (ambient) aerosol distributions derived from CAS observations from only the below the cloud base flight legs. Above cloud base and below cloud top legs are used for analysis in section 3.3. We use 1 Hz data for 75 flights on 43 different dates from January to June 2022. Each 1 Hz observation is taken from a typical 3 minute below cloud base (BCB) flight leg and only samples passing our clear sky filtering criteria are retained. Though the CAS measures particles at 0.5 μm to

https://doi.org/10.5194/egusphere-2026-3027
Preprint. Discussion started: 16 June 2026

50 μm diameter, we select only measurements corresponding to haze particles (ambient hydrated particles) ranging from 2.5 μm to 50 μm diameter for both the CAS and CDP, which removes any accumulation mode particles before constructing our distributions. The CDP range is 2.5 μm to 50 μm diameter. It is important to note that this ambient size, for most RH values sampled, corresponds to a dry minimum diameter of less than 2 μm, which ensures that we capture all the sea spray particles with dry diameters greater than 2 μm, even as the RH varies along each flight leg. After the removal of flight legs exceeding clear-sky filtration process (see section 2.1), the relative humidity analysis yielded 460 below cloud base legs with a mean altitude of 701 m. To contextualize our ambient (haze) size distributions, we compare our average ambient CAS and CDP distributions with Lewis and Schwartz (2004). We compare with their Fig. 22b, which shows a range of average size distributions across multiple studies at an average wind speed of 5-7 m s^{-1}, shown in Figure 1. Although Lewis and Schwartz (2004) report size distributions across a broader range of wind speeds, our comparisons are limited to the 5-7 m s^{-1} range, which is closest to the mean wind speed observed in our dataset (5.13 m s^{-1}) and contains the most robust sampling. Higher wind speed regimes reported in previous studies are not well represented in our dataset, limiting direct comparison. Their distributions are reported at 80% RH (r_{80}), so we normalize our ambient measurements to this reference humidity using a hygroscopic growth factor derived from the mean relative humidity of each flight leg (see below). The resulting r_{80} values are used to rescale particle sizes while maintaining the measured number concentration distributions. All size distributions used for this comparison are in $\frac{dN}{dlnD}$ to maintain consistency with Lewis and Schwartz (2004). We find that our CDP and CAS ambient distributions in this wind speed range, normalized to r_{80}, generally fall within the 3 standard deviations of the studies depicted in Lewis and Schwartz Fig. 22b.

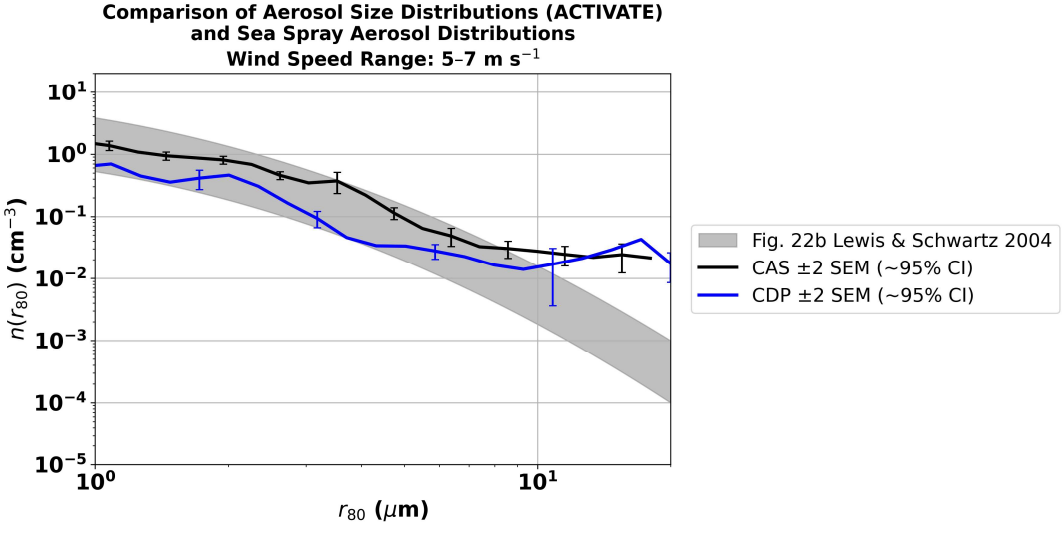

Figure 1 Normalized average ambient aerosol size distributions measured by the CAS (black) and CDP (blue) during ACTIVATE flights for wind speeds of 5-7 m s^{-1}. Error bars denote +/-2 standard errors (95% confidence interval)

https://doi.org/10.5194/egusphere-2026-3027
Preprint. Discussion started: 16 June 2026

based on variability across contributing flight legs (see section 2.3 for details). The grey shaded region represents the range of sea spray aerosol size distributions compiled from multiple studies by Lewis and Schwartz.

We estimate dry salt aerosol size distributions from our hydrated measurements. To convert an ambient size distribution to a dry salt size distribution, we utilize the average flight leg's relative humidity with respect to liquid water, taken from the Diode Laser Hygrometer (DLH) aboard the Falcon (Diskin et al., 2002; Sorooshian et al., 2023), and the corresponding salt particle "growth factor" (Seinfeld and Pandis 2006). The hygroscopic growth factor quantifies how aerosol particles absorb moisture from the atmosphere, leading to an increase in their size. This growth factor $g(RH)$ is approximated with a simple fit based on the formulation from Tang et al. (1997) as:

$$g(RH) = \left(\frac{1.7}{1-RH}\right)^{0.31}, \quad (1)$$

The growth factor $g(RH)$ is a function of leg-mean relative humidity (RH) only (for coarse mode sea spray particles, assuming constant sea spray composition), not of diameter and therefore varies across all flight legs (Tang 1996; Jensen and Lee 2008). Ambient particle diameters are converted to dry diameters by dividing by $g(RH)$, and the corresponding number size distributions, expressed as $\frac{dN}{dD}$, are transformed into dry-diameter space. Since RH differs across flight legs, the resulting dry diameter bins vary slightly; therefore, each dry size distribution is interpolated onto a common dry diameter grid spanning 2 to 25 μm before averaging. Average dry size distributions for each instrument are compared in Figure 2. We calculate the mean total concentration for the CAS to be 0.56 cm^{-3} and 0.18 cm^{-3} for the CDP.

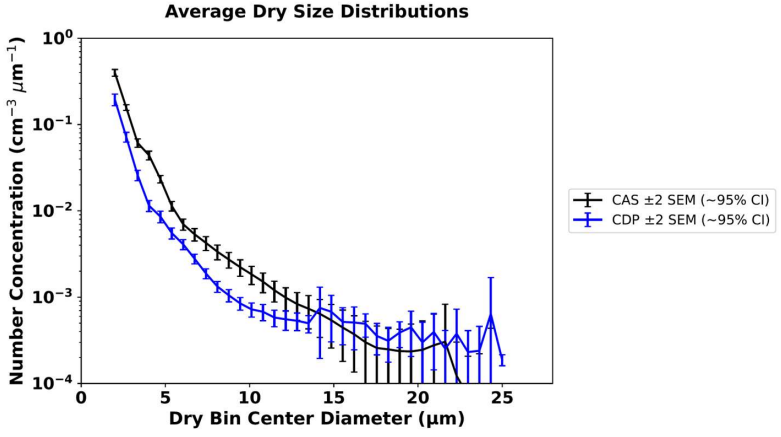

Figure 2 Average dry aerosol size distributions derived from CAS (black) and CDP (blue) measurements. Error bars represent +/-2 standard errors of the mean (95% confidence interval) based on variability across contributing flight legs (see section 2.3 for details) for January-June 2022 below cloud base flight legs.

The flight legs in this study from ACTIVATE averaged a sample time of 180 seconds, which is relatively short compared with some other studies (Cólon-Robles et al., 2006 used circle legs of ~30-minute duration). Low particle

https://doi.org/10.5194/egusphere-2026-3027
Preprint. Discussion started: 16 June 2026

counts can result in "shot noise" and a flattening of the size distributions for the lower concentrations of larger sized particles (Baumgardner et al., 2017). To quantify this effect, because low particle counts at larger diameters lead to elevated shot noise, we estimate the relative Poissonian counting error for each size bin using Eq. (2):

$$relative\ error\ = \frac{\sqrt{N_{counts}}}{N_{counts}}, \quad (2)$$

This allows us to identify the particle sizes for which the counting statistics are most reliable. Because of the quasi-exponential nature of the coarse mode size distributions and the limited probe sampling volume, the relative error exceeds 100% for many bin diameters above ~10 μm in many cases, so we choose to limit our exponential fitting (See equation 2) to the portion of each distribution smaller than 10 μm diameter. The fitted parameters ($N_{0,\,dry}$ and $D_{e,dry}$) (See equation 2) and their covariance provides insight into how the abundance (concentration), characteristic size, and the overall mass of coarse-mode aerosol vary together for both instruments, illustrated in Fig. 3.

One possible method to work with "shot noise" is to concatenate a set number of individual 3-minute legs into "super legs" to create legs with longer sampling time. However, because the typical ACTIVATE sampling approach mostly involves sampling the different air masses on subsequent legs due to minimal backtracking, changing meteorological conditions would result in "super leg" averages that mix air from numerous locations. The number of legs logged per flight per day varies strongly (between 2-16 legs) and concatenating across multiple legs, flights, or days would risk introducing additional variability due to changing meteorological and flight conditions. Instead, to smooth shot noise, we fit an equation of exponential decay to each size distribution using Eq. (3):

$$n(D_{dry}) = N_{0,\,dry} e^{-\frac{D_{dry}}{D_{e,\,dry}}}, \quad (3)$$

where $N_{0,\,dry}$ represents the intercept and $D_{e,dry}$ represents the e-folding diameter, which controls the fall-off in concentration with size. This fit is performed using nonlinear least-squares regression, such that all included size bins contribute equally to the regression. As a result, bins with low particle counts, like those at larger diameters, may be subject to greater statistical uncertainty due to counting variability. To mitigate the influence of this "shot noise", the fitting is restricted to dry diameters ≤10 μm, where particle counts are higher and sampling uncertainty is reduced. The fitted parameters derived from these dry size distributions are further used for analysis in section 3.2. The slope parameter from these fits, displayed in Figure 3, provides a useful framework for looking at how variations in size distribution influence aerosol properties such as number concentration and mass.

https://doi.org/10.5194/egusphere-2026-3027
Preprint. Discussion started: 16 June 2026

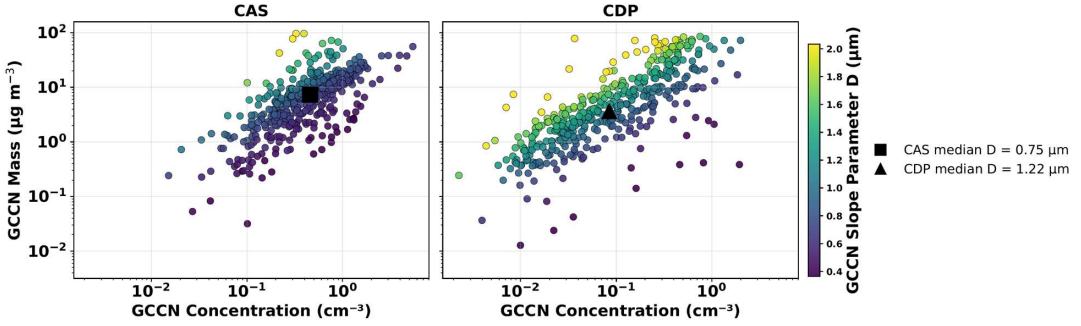

Figure 3 shows the relationship between GCCN dry mass and number concentration CAS and CDP observations. Each point is colored by the fitted slope parameter $D_{e,dry}$, which characterizes the e-folding diameter of the dry size distribution.

Larger values of D correspond to distributions with relatively more large particles. A strong positive relationship is observed for both instruments, with most points falling near a "slope of one" trend, indicating that increases in particle number are generally accompanied by increases in total mass. Although both instruments show a strong positive relationship between number concentration and mass, notable differences are evident between the CAS and CDP observations. The CAS exhibits a slightly steeper relationship than the CDP. The total mass values from the two probes are generally similar, differing by roughly a factor of two, whereas the number concentrations differ more substantially, by up to a factor of five. In particular, lower concentrations, ~10^{-2} cm^{-3}, are observed more frequently for the CDP than the CAS. The CDP also tends to have larger values of $D_{e,dry}$, which correspond to a slower decrease in concentration with size. As a result, although the CDP measures fewer particles overall, these particles tend to be larger to compensate for the lower number concentration. This also yields total mass values that are more comparable to those observed by the CAS.

2.3 Wind speed binning

Near surface wind speed has been shown to be one of the leading controlling factors on bubble bursting and the production of sea spray aerosol (Woodcock 1953; Monahan et al. 1986; Banner and Peregrine, 1993; Gemmrich and Farmer, 1999; Clarke et al., 2006). To explore the relationship between wind speed and coarse-mode aerosol concentration for aerosol dry diameters larger than 2.0 μm, which we define as $N_{d>2}$, we first apply a logarithmic wind profile correction (Stull 1988) to all Falcon in-situ wind speed measurements, standardizing them to 10 m above sea level. Wind speeds were collected from the NASA Langley in situ aircraft state dataset which provides aircraft-derived wind measurements (Sorooshian et al., 2023). This correction accounts for variability in flight leg altitude and uses a roughness length of 0.02 m for open ocean conditions (Peña and Gryning 2008). The mean 10 m wind speed across all valid below-cloud-base legs is 5.13 m s^{-1} with a standard deviation of 2.65 m s^{-1}.

https://doi.org/10.5194/egusphere-2026-3027
Preprint. Discussion started: 16 June 2026

Due to the relatively short flight legs in ACTIVATE, we aggregate flight legs into six wind speed bins that capture the full range of observed wind speeds (Fig. 4). Previous observational studies have shown a strong dependence on wind speed for aerosol concentration, particularly in the coarse mode (Woodcock 1953; Lewis and Schwartz 2004; Colón-Robles et al. 2006). Given this established dependence, grouping legs by wind speed allows us to directly compare our results with prior findings (section 4) while increasing the statistical robustness of our results, as the aggregation reduces variability from short sampling times. These bins are designed to represent the overall wind speed range in our dataset, 0 m s^{-1} to 16 m s^{-1}. The selected wind speed ranges are 0–2.5, 2.5–3.5, 3.5-5, 5-7, 7-9, and >9 m s^{-1}, which we manually selected. The distribution of 10 m wind speeds in our dataset is not uniform. The chosen ranges (0–2.5, 2.5–3.5, 3.5–5, 5–7, 7–9, and >9 m s^{-1}) ensure that each of the 6 bins contains a sufficient number of flight legs while also isolating wind speed ranges commonly discussed in sea spray aerosol literature (Lewis and Schwartz 2004, see Fig. 1). We repeated the analysis using smaller binning schemes, 4 and 5 wind speed bins (not shown), and found that the slope of the concentration and wind speed relationship differed by less than 16% compared to the 6-bin case, with all slopes overlapping within their respective uncertainties.

We examine the dependence of coarse-mode aerosol concentration $N_{d>2}$, cm^{-3}, and mass, $M_{d>2}$, $\mu g\ m^{-3}$, on wind speed by analyzing binned number concentration and mass as a function of wind speed for both the CAS and CDP (Fig. 4). Using both the CAS and the CDP enables us to evaluate whether the observed relationships hold consistently across different instruments. We take the mean dry size distribution, resulting in one average size distribution for each of the six wind speed bins, shown in Fig. 4 for GCCN concentration. The standard error quantifies the uncertainty in the mean droplet concentration at each particle size bin due to the finite number of legs within each wind speed range. Size distributions are in $\frac{dN}{dD}$ and standard error is calculated following Eq. (4):

$$SE = \frac{\sigma}{\sqrt{n}}, \quad (4)$$

where σ represents the standard deviation calculated across all flight legs within a given wind speed bin at each particle size bin, and n represents the number of flight legs included in that bin. In addition to computing standard error for our wind speed and concentration and relationships, we also compute counting errors for total concentration measured by each instrument. Counting uncertainties are assumed to follow Poisson statistics, where the uncertainty in particle counts is given by the square root of the number of counts. These uncertainties are propagated to concentration by accounting for the instrument sample volume. The total counting error is obtained by adding the bin-level errors in quadrature, which reduces to:

$$\delta N = \sqrt{\sum_i C_i}, \quad (5)$$

where δN is the total counting error in the integrated concentration, N is the total concentration obtained by summing over all size bins, and C_i is the concentration in bin i. The bin concentrations , C_i are calculated as the product of the mean size distribution and the bin width, δd_i.

While number concentration captures the abundance of coarse-mode aerosol particles, quantifying the mass dependence on wind speed allows us to determine whether higher wind speeds produce larger particles. Following the

https://doi.org/10.5194/egusphere-2026-3027
Preprint. Discussion started: 16 June 2026

same method of analysis from our wind speed versus concentration relationships, we maintain the same 6 wind speed bins and mean size distributions in each bin. The total dry mass in each wind speed bin was calculated from the mean size distributions as:

$$M_{d>2} = \frac{\pi}{6}\rho_{salt}\sum_{i=D_{i>2\,\mu m}} C_i D_i^3, \quad (6)$$

where $M_{d>2}$ is the total dry mass in each wind speed bin, μg m^{-3}, C_i is the concentration in bin i, D_i is the particle diameter of bin i, and the density of salt (ρ_{salt}) is 2200, kg m^{-3}. Standard error is calculated in each bin following Eq. (4). Additionally, we compute instrument counting error for mass for both instruments following Eq. (7):

$$\delta M_{d>2} = \frac{\pi}{6}\rho_{salt}\left[\sum_{i=D_{i>2\,\mu m}} D_i^6 C_i\right]^{\frac{1}{2}}, \quad (7)$$

where $\delta M_{d>2}$ is the counting error in total mass. This formulation explicitly accounts for the influence of larger particles through the diameter term on both the mass and its associated uncertainty. Counting uncertainties in mass are small for both instruments, although they are larger than for concentration, as mass is influenced by the largest particles, even if they are less numerous. However, these counting errors still remain much smaller than the leg-leg variability represented by the standard error, further showing that mass is not dominated by limitations in particle counting.

We make sure to remove flight legs for which the average mass exceeded 100 μg m^{-3}. These values represent extreme outliers relative to the typical range of observed GCCN mass and likely reflect measurement artifacts or anomalous sampling conditions. Excluding these cases prevents a small number of unusually large values from disproportionately influencing the statistical analysis. The resulting mean dry mass for the CAS is 10.3 μg m^{-3} (median = 7.4 μg m^{-3}) and 12.2 μg m^{-3} (median = 3.6 μg m^{-3}) for the CDP (Fig. 3).

2.4 Microphysics Model

To assess the potential role of giant cloud condensation nuclei (GCCN) in warm rain formation, we use a condensational and collisional super droplet model (Shima et al. 2009) to simulate cloud droplet evolution from the cloud base to cloud top. A column of air is lifted (details are provided below), resulting in saturation and condensational growth, followed by collision-coalescence and rainout. Haze particles grow, and a fraction activates to form cloud droplets as they are lofted above the cloud base, allowing us to determine their influence on cloud microphysics and precipitation initiation. This Lagrangian model tracks the growth of any specified dry aerosol size distribution, which may include a supermicron (GCCN) distribution. Multiple droplets are represented by a single computational particle with attributes including the multiplicity, the dry size, the wet size, and the location.

Since the model is stochastic, we use an ensemble size of 16 for each case, with 20,200 super droplets across the whole cloud. The cloud thickness is 400 m, representing a typical precipitating warm cloud. The submicron aerosol is represented with a log-normal distribution with a fixed median radius of 0.1 microns and a fixed geometric standard deviation of 1.835, consistent with the 7th modal aerosol module (MAM7) from the 5th Community Atmosphere

https://doi.org/10.5194/egusphere-2026-3027
Preprint. Discussion started: 16 June 2026

Model (CAM5) (Liu et al. 2012), except to avoid complicating the activation process, we only simulate particles larger than 0.1 micron in radius.The updraft velocity, w, as a function of time is given by Eq. (8), which linearly decreases to zero by t = 800 s:

$$w_{(t)} = w_0\left(1 - \frac{t}{800\ s}\right)\ \ if\ \ t < 800\ s \text{ else } 0, \quad (8)$$

There is no downdraft in this simulation. w_0 represents the peak updraft speed (1 m s^{-1}). The resulting vertically integrated liquid water path (LWP) after lifting is about 385 g m^{-2}, which is representative of the thicker parts of marine boundary layer clouds that are likely to be precipitating (Rémillard et al., 2012). The simulation assumes an initially uniform RH of 99%. The column has a uniform pressure of 1000 hPa and a uniform temperature of 300 K. With such a thin cloud, this is a decent approximation. Pressure changes and latent heating are neglected. These conditions produce a LWP of 385 g m^{-2} which is deemed the "base" LWP for these simulations, but we also incorporate sensitivity tests with a low LWP of 100 g m^{-2} for simulations to explore the dependence of precipitation on GCCN in thinner clouds (section 3.2).

The submicron aerosol number concentration for the base case is set to 50 cm^{-3}, which is typical of relatively clean marine conditions (Heintzenberg et al., 2000), but we also vary this from 10 cm^{-3} to 100 cm^{-3} to explore sensitivity to background submicron aerosol concentrations. Particles in the accumulation mode *and* coarse mode are assumed to be hygroscopic (hygroscopicity parameter, "kappa", of 0.7, Petters and Kreidenweis 2008). For any desired kappa, we use the transformation $r^3 = 0.7r^3/kappa'$ to find the corresponding effective dry radius. Using the parametric collision kernel given by Ayala et al. (2008) and the ordinary Hall collision efficiencies, we choose two representative levels of turbulence defined by the eddy diffusivity: 0 $cm^2\ s^{-3}$ (no microscale turbulence) and 50 $cm^2\ s^{-3}$. For turbulent cases, the Taylor-microscale Reynolds number is fixed at 75.

As the model runs, particles remain within the column, where the updraft initiates their growth via condensation upon reaching supersaturation. They continue growing for 800 seconds, after which the updraft ceases and drops sediment out. Both condensation and collision coalescence can take place throughout and after the ascent. The total simulation length is 1 hour, selected as a typical cloud lifetime, and the vertical resolution is 25 m. Particles are initially uniformly distributed in height. Precipitation is measured as the mass of drops that reach below the cloud base with radii greater than 30 microns. This threshold is meant to estimate in a real cloud which particles can reach the surface before evaporating.

The goal of these simulations is to determine the effect of GCCN on precipitation, both in terms of mass of GCCN and total concentration of GCCN. For computational efficiency, we use size distributions from only one instrument, the CAS. The masses for the CAS and CDP, and how mass and number depend on each other are quite similar (Fig. 3). So, running the simulations on both instruments would likely yield similar results. We use all 460 flight leg dry size distributions to serve as model input. We extract the slope and intercept parameters from exponentially fitted dry size distributions (section 2.2), and compute the total coarse-mode dry mass of sea salt (μg m^{-3}) for each GCCN size distribution using Eq. (8). Coarse-mode dry GCCN mass M_{dry} is determined as:

https://doi.org/10.5194/egusphere-2026-3027
Preprint. Discussion started: 16 June 2026

$$M_{dry} = \frac{\pi}{6}\rho_s N_{0,dry} \int_{(D_{dry})_{min}=2\ \mu m}^{\infty} (D_{dry}{}^3) e^{-\frac{D_{dry}}{D_{e,dry}}} dD_{dry}, \quad (9)$$

The density of sea salt, ρ_s, is 2200 kg m^{-3}, M_{dry} is the total dry mass concentration per flight leg (expressed in units of μg m^{-3}), $N_{0,dry}$ is the dry intercept, $(D_{dry})_{min}$ is the minimum dry diameter, D_{dry} is the dry diameter (μm), and $D_{e,dry}$ is the e-folding diameter previously extracted from the exponential fit to the dry size distributions.

3 Results

3.1 Wind speed influence on coarse-mode aerosol concentration and mass

Both concentration and mass increase with wind speed, indicating enhanced production of coarse-mode particles under stronger surface winds (Fig.4). However, substantial variability exists within each wind speed bin, suggesting that wind speed alone does not fully constrain the observed aerosol properties. A similar positive relationship observed between coarse-mode mass and wind speed for both instruments. The relationship between mass and wind speed also shows a statistically significant relationship for both instruments, with fitted slopes of $0.63 +/-0.51$ and $0.31 +/- 0.29$ μg m^{-3} for the CAS and CDP, respectively, and coefficients of determination of $R^2 = 0.61$ and $R^2 = 0.54$. While both mass and concentration increase with wind speed, the large error bars show that substantial variability remains between flight legs.

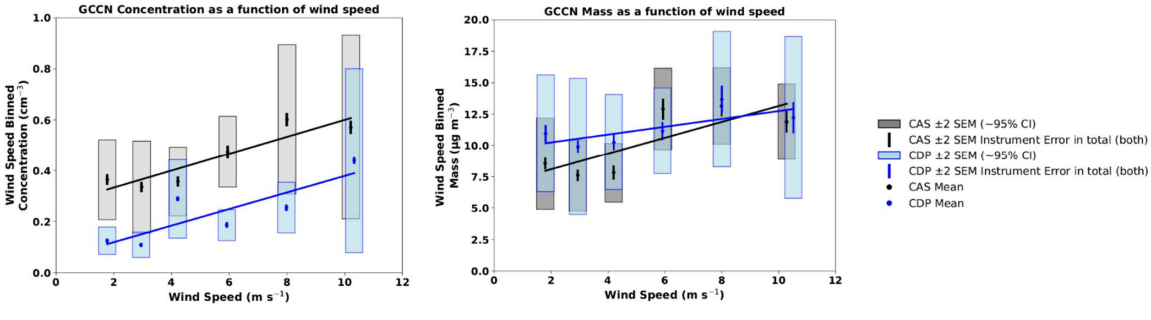

Figure 4 Relationship between wind speed and number concentration, $N_{d>2}$, (left) and GCCN dry mass, $M_{d>2}$, (right). Data are grouped into six wind speed bins, and each point represents the mean value derived from the average dry size distribution within each bin. Shaded boxes denote +\-2 standard errors of the mean (95% confidence interval) across the flight legs contributing to each bin, while vertical bars represent +/- 2σ instrument counting error propagated through the integrated mass or concentration calculation. Black symbols correspond to CAS measurements and blue

https://doi.org/10.5194/egusphere-2026-3027
Preprint. Discussion started: 16 June 2026

symbols correspond to CDP measurements. Solid lines indicate linear least-squares fits to the binned means and are reported in Table 1.

Statistics for wind speed binned GCCN mass and concentration

Variable	Instrument	Slope ± 2 SE (95% CI)	Int. ± 2 SE (95% CI)	R^2
Mass	CAS	0.63 ± 0.51	7 ± 3	0.61
Mass	CDP	0.31 ± 0.29	10 ± 2	0.54
Concentration	CAS	0.033 ± 0.015	0.3 ± 0.1	0.84
Concentration	CDP	0.029 ± 0.022	0.1 ± 0.1	0.64

Table 1 Linear regression statistics describing the relationship between wind speed and wind-speed-binned GCCN dry mass and number concentration for CAS and CDP measurements. Slopes (m) in units of μg m^{-3} per m s^{-1}, intercepts (b), and coefficients of determination (R^2) are derived from least-squares fits of the form $y = mx + b$ applied to the mean values within each wind speed bin. The slopes for both GCCN mass and concentration are positive for both instruments. While all slopes are statistically significant at the 95% CI, the large uncertainties associated with the mass relationships, particularly for CDP, indicate a more variable dependence on wind speed.

The slopes for the concentration-wind speed fits (Fig. 4 for the CAS and CDP respectively (Table 1)), uncertainties represent +/-2 standard errors of the mean (SEM; 95% CI). The slopes agree within statistical uncertainty. Furthermore, the overall relationship between $N_{d>2}$, of individual flight legs and wind speed for both instruments show statistically significant (Table 1) consistent positive trends, with increasing concentrations at higher wind speeds. Coefficients of determination are $R^2 = 0.84$ and $R^2 = 0.64$ for the CAS and CDP, respectively. However, there is substantial variability between flight legs, reflected in the large error bars, demonstrating consistence with prior studies (e.g. Colón-Robles et al 2006) that wind speed alone does not fully explain the observed variability in GCCN concentrations.

3.2 Modeling GCCN influence on precipitation

To evaluate how variability in observed GCCN properties influences precipitation, we apply the model across the full set of flight-leg size distributions. The resulting relationships between accumulated rainfall and GCCN concentration and mass are shown in Fig. 5.

https://doi.org/10.5194/egusphere-2026-3027
Preprint. Discussion started: 16 June 2026

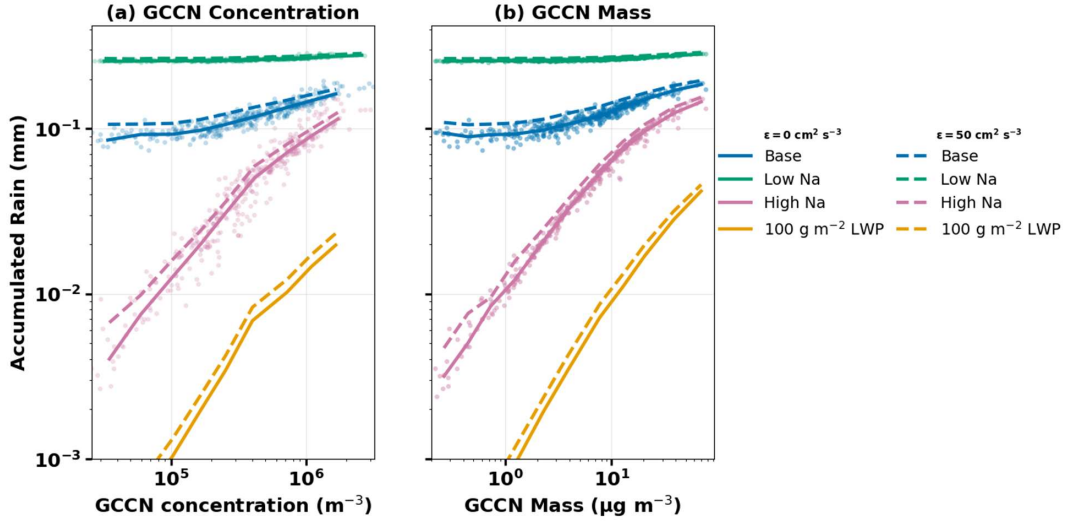

Figure 5 1-D kinematic super droplet microphysics model simulations showing accumulated rainfall over the 1 hr simulation, as a function of GCCN concentration ($N_{d>2}$) (a) and GCCN mass ($M_{d>2}$) (b). Model simulations were performed for all flight legs. For the "base" simulation ensemble (blue), the liquid water path is fixed at 385 g m^{-2} and the submicron aerosol concentration N_a is 50 cm^{-3}. Also shown are low LWP (100 g m^{-2}) simulations with the same N_a (yellow). Two levels of turbulent dissipation rate (ε = 0 and 50 cm^2 s^{-3}) are shown in each ensemble to represent increasing levels of turbulence. High N_a ensembles use a concentration of 100 cm^{-3} and low N_a ensembles use a concentration of 10 cm^{-3}. Colored curves show the binned median responses for each ensemble, while the scatter points represent model estimates using individual flight legs. The median response provides a representative description of the ensemble behavior.

The simulations show a clear and consistent enhancement of accumulated rainfall with increasing GCCN mass (Fig. 5a) and concentration (Fig. 5b). Across all model ensembles, median accumulated rainfall increases systematically with GCCN concentration or mass, showing that higher GCCN levels are associated with more efficient warm-rain production over the one-hour simulation. This behavior is seen in the median curves, as well as, in the distribution of individual flight-leg simulations, represented by the scatter. The scatter from the full set of flight legs closely follows the log-binned median response in both panels. This agreement is important because it shows that the relationships in Fig. 5 reflect a consistent response across the full population of observed GCCN size distributions.

The low N_a (10 cm^{-3}) ensembles of simulations consistently produce the most rainfall over the simulation, for a given GCCN concentration ($N_{d>2}$, Fig 5a) or mass ($M_{d>2}$, Fig 5b). In contrast, the high N_a simulations produce considerably less rainfall, with the "base" ensemble lying below these two limits. The sensitivity of the rain to $N_{d>2}$ and $M_{d>2}$ is much stronger, in a relative sense, for higher aerosol background (larger N_a). This demonstrates that the background aerosol environment of the simulations clearly influences not only the precipitation (as is expected from numerous

https://doi.org/10.5194/egusphere-2026-3027
Preprint. Discussion started: 16 June 2026

previous observational and modeling studies), but also helps set the effectiveness of GCCN in influencing warm rain. Under low N_a conditions, the cloud contains fewer competing smaller droplets, which leads to more effective collision-coalescence of droplets, leading to enhanced rainfall. The high N_a ensemble conditions distribute available water across a larger number of droplets, slowing the rate of accumulated rainfall. The shape of these curves is also important. For the low N_a ensembles, rainfall increases at a slower rate with GCCN mass and concentration and tends to weaken somewhat at the highest values, particularly for concentration (Fig. 5a). This implies that continuing to add more GCCN can yield smaller additional increases in accumulated rain at a certain point, (or possibly even drop off). In contrast, accumulated rainfall for the high N_a and "base" ensembles appear to increase more rapidly with $N_{d>2}$ and $M_{d>2}$ when GCCN levels are low. This is consistent with how the low-LWP ensembles also increase rapidly with GCCN levels, but the rain remains very small ($<10^{-2}$ mm in an hour) until GCCN loadings increase significantly. The limited liquid water available in these conditions initially suppresses droplet growth and hinders collision-coalescence between the droplets formed on submicron aerosol and also the tail of growing GCCN particles accreting cloud droplets. The presence of GCCN alone is not enough to generate rainfall if the available liquid water is limited.

Furthermore, in both panels (Fig 5), increasing GCCN is associated with more accumulated rainfall, but the correlation with GCCN mass ($M_{d>2}$) is significantly tighter than for number concentration $N_{d>2}$, as seen with the individual simulations for flight leg averages (circles in Fig. 5). This is particularly evident in the low LWP ensemble, where higher GCCN mass produces greater accumulated rainfall than comparable increases in number concentration. These larger particles accelerate the growth of precipitation sized drops, leading to greater accumulated rainfall. Finally, the influence of microscale turbulence on the collection kernel rate is also important, although more subtle than the effect of background conditions and GCCN. For all ensembles, the median rain accumulation curves for both turbulence levels remain closely clustered together, indicating that the overall trend of the GCCN rainfall relationships is robust across the range of dissipation rates given. However, it is clearly seen that increased level of turbulence increases rain rates across all ensembles. Microscale turbulence (as represented here by turbulent dissipation rate) impacts the efficiency of droplet growth and collision-coalescence, by increasing the likelihood of collisions between droplets. For reasons that are not entirely clear, the relative impact of microscale turbulence is greatest for the base N_a ensemble, and is also most important at the lower precipitation rates, where it can help overcome the barrier to precipitation formation caused by cloud droplets that are too small to effectively collide (high N_a). Overall, the behavior of the ensembles show that the magnitude of rainfall is dependent not only on the size and number of particles, but on the amount of available cloud water.

3.3 Observations of GCCN influence on precipitation

While the model results in section 3.2 illustrate theoretically how giant CCN can accelerate precipitation rates, it is difficult to provide a direct comparison with the model due to sampling challenges with the dataset. ACTIVATE lacks a radar measurement collocated with the GCCN observations, and the majority of the flight legs are undertaken in a survey-type mode rather than providing repeated sampling of an air mass at different levels. These limitation makes the dataset less amenable to closure studies that focus specifically on relating precipitation to cloud and aerosol

https://doi.org/10.5194/egusphere-2026-3027
Preprint. Discussion started: 16 June 2026

variability. Instead, we can use aircraft in situ sampling of rain water content (RWC), together with cloud water content (CWC), and cloud droplet concentration (N_d) and develop a composite analysis that is used to assess whether flights with high GCCN concentrations (or mass) contain more or less precipitation than those with low GCCN levels. Rainwater content (RWC) is a direct measure of the condensate converted into precipitation-sized drops, making it a key proxy for evaluating the role of GCCN in affecting the cloud to rain conversion. To isolate the role of GCCN, we analyze RWC within set bins of LWC and N_d, which constrain the cloud macrophysical and microphysical state and hold it constant. This allows us to evaluate the effect of GCCN mass and concentration on RWC while minimizing the potentially confounding influence of background cloud variability. So, in addition to using the modeling described in section 3.2, we use the in situ measured cloud and precipitation size distribution to derive observational estimates of rainwater content and total liquid water content, which is defined as:

$$LWC = RWC + CWC \quad (9)$$

We set a threshold diameter of 50 μm to separate cloud from rain drops (Glienke et al., 2017; Sanchez et a., 2023). As we saw in the ensemble simulations (Fig. 5), GCCN can accelerate collision-coalescence, which manifests in an increased rate of conversion of CWC to RWC (Posselt and Lohmann 2008). It is widely appreciated that the rate of conversion of cloud to rain in a cloud is strongly dependent upon the amount of condensate produced in an updraft by condensation (LWC), and is sensitive to the cloud droplet concentration, N_d, as higher droplet numbers suppress precipitation formation by limiting droplet growth (Berry and Reinhardt 1974; Khairoutdinov and Kogan 2000; Wood 2005b). ACTIVATE does not have aircraft remote sensors that provide liquid water path (LWP) measurements. Instead, we can use the total LWC, provided in Eq. (10) as the sum of the CAS or CDP CWC and the 2D-S RWC (precipitation water), where the 2D-S RWC is calculated using only bins with diameters greater than 50 μm to avoid double counting.

Our analysis here is carried out using 1 Hz in-cloud data from the CAS, CDP, and 2D-S because coalescence tends to be strongly spatially variable, so the use of leg means is inappropriate. To gather in-cloud data, we take measurements from above cloud base legs (ACB) and below cloud top legs (BCT), both of which focus on cloud sampling. The ACB and BCT legs are combined into a unified dataset. We compute a total in-cloud number concentration N_d from the CAS or CDP, along with CWC and RWC estimates from the CAS or CDP and 2D-S respectively for every second of cloudy data. In-cloud conditions from the CAS or CDP are identified using a CWC threshold >0.01 g m^{-3}, ensuring that only data points within cloud are considered. Raindrop number concentration is also estimated but are 2-3 orders of magnitude smaller than N_d and therefore do not contribute substantially to total droplet concentration. RWC estimates use bins with diameters of 62.70 μm to 1464.90 μm captured from the 2D-S via the following Eq. (10):

$$RWC = \frac{\pi}{6} \times \rho_w \sum_{i=6}^{128} n_i \times {D_i}^3 \Delta D_i \quad (10)$$

The density of water, ρ_w =1000 g m^{-3}, n_i is the observed, binned size distribution (dn/dD) in bin i, D_i is the bin central diameter, and ΔD_i is the bin width. The 2D-S has 128 bins, but the first 5 are highly uncertain due to poorly-defined sizing and sample volume for the smallest rain drops, and these are not used. The smallest 2D-S bins also overlap with the largest CAS and CDP bins, so our approach also avoids the potential for double counting. The CWC and RWC are summed to compute the total liquid water content (g m^{-3}) per second, Eq. (11).

https://doi.org/10.5194/egusphere-2026-3027
Preprint. Discussion started: 16 June 2026

To analyze the fractional contribution of rainwater to the total liquid within the cloud, we compute the percentage ratio of rainwater to total condensate:

$$\xi = \frac{RWC}{LWC} \times 100 \quad (11)$$

All the flights and legs used for the previous analysis are included. Based on our understanding of precipitation formation, ξ will increase as the total condensate level increases and is expected to also be higher for low N_d. By controlling for these variables, we can then investigate the potential sensitivity to GCCN mass and number concentration (as is suggested by the microphysical modeling, section 3.2). To control for these variables, we place ξ into discrete bins of LWC and N_d. These bins are logarithmically spaced (4 in each dimension to give 16 total bins) to capture observed variability. We then take the mean RWC and LWC in each of the bins and compute ξ as the ratio of these means, i.e., $\xi(LWC, N_d) = \overline{RWC}/\overline{LWC} \times 100$. The mean N_d over all cloudy data is 125 cm^{-3} (10th-90th percentile: 15-235 cm^{-3}), and the mean LWC is 0.17 g m^{-3} (10th-90th percentile: 0.047-0.32 g m^{-3}).

As expected, high LWC and lower N_d are two primary controls on rainwater content (Fig. 6), so we can use this as a framework to evaluate the potential impact of GCCN on RWC. However, this analysis does not currently isolate the impacts of GCCN on this specific measure of precipitation efficiency, defined here by the ratio of RWC to LWC. The model results (section 3.2), showed that, while both GCCN number concentration and mass impact precipitation, mass seems to have a better correlation than number concentration. We perform our observational rainwater content analysis for both GCCN variables. To do this, we subdivide the dataset into cases with high and low GCCN mass $M_{d>2}$ (and a separate split for GCCN number concentration $N_{d>2}$). We use our previously calculated leg-mean GCCN $M_{d>2}$ (section 2.3). Because the cloudy data cannot be precisely collocated with the out-of-cloud GCCN measurements, which are also made using different flight legs, and flights are relatively short, we decided to use the flight-mean GCCN mass (across all legs used to determine means for each flight) and then assign all the cloud data from the cloudy legs from that flight as high or low GCCN clouds on the basis of the flight mean GCCN concentration, depending on the analysis. We produce an average GCCN mass for each of our 75 flights. To categorize each flight, we take the top 50% of flight mean $M_{d>2}$ (or $N_{d>2}$) (37 flights) as "high" GCCN and the bottom 50% (38 flights) as "low". To assess the robustness of our results using 50% split categories, we repeated the same analysis with a “high” category of the top 20% of flights and a “low” category of the bottom 20% of flights. We also tested a “high” category of the top 40% of flights and a “low” category of the bottom 40% of flights (not shown). We then separate the calculated RWC data into high and low GCCN flight categories (Fig. 7).

RWC is evaluated as a function of total LWC and N_d for both the “high” and “low” GCCN categories and a clear increase in RWC/LWC is observed in the high GCCN category relative to the low GCCN category (Fig. 7). Ratios were calculated only in bins where the combined number of available cloudy 1 Hz data points across the high and low GCCN subsets is greater than or equal to 100, depicted in Fig. 7; bins that did not meet these criteria are masked. This visualization provides a normalized metric for comparing the relative impact of GCCN under varying cloud conditions.

https://doi.org/10.5194/egusphere-2026-3027
Preprint. Discussion started: 16 June 2026

To assess the statistical significance of RWC/LWC differences between high and low GCCN conditions (either using $M_{d>2}$ or $N_{d>2}$ to characterize GCCN) we applied a bootstrap resampling approach within each joint N_d and LWC bin. Bootstrapping is well suited for this analysis because the flight-mean data are unevenly distributed across bins and may not follow a normal distribution, violating assumptions of traditional parametric tests. For each bin, we generated 10,000 bootstrap realizations by resampling flight legs with replacement separately for the high and low subsets. For each realization we computed the ratio of mean RWC/LWC between the two groups, producing a distribution of possible outcomes for each bin. This resulted in a distribution of possible outcomes per bin, from which we computed 90% confidence intervals, mean and median values, and the percentage of bootstrap samples indicating an enhancement in RWC/LWC in the presence of GCCN.

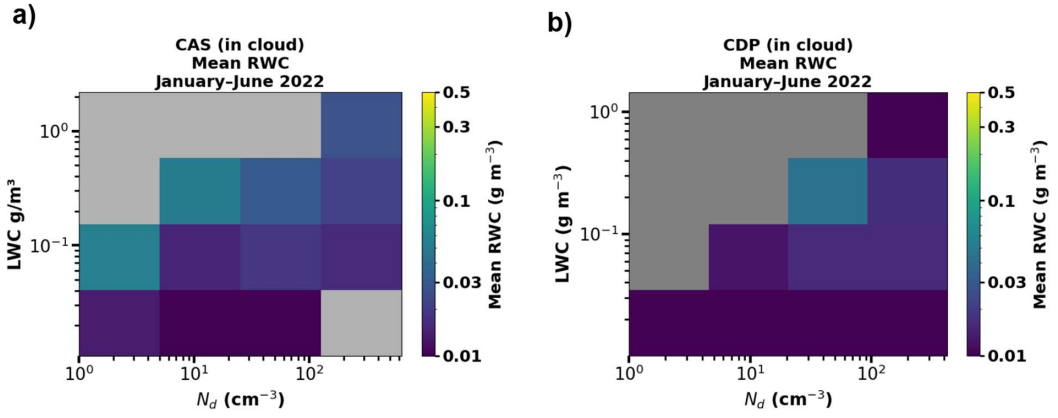

Figure 6 Mean RWC as a function of LWC and N_d for the CAS (a) and the CDP (b). Dark purple indicates lower mean RWC and light blue to yellow indicates higher mean RWC. Gray bins indicate bins where fewer than 100 valid data points are available across the compared subsets and are excluded from analysis. For both instruments, highest levels of mean RWC are observed for moderate LWC-N_d. We found our analysis not to be sensitive to the choice of percentile threshold used.

https://doi.org/10.5194/egusphere-2026-3027
Preprint. Discussion started: 16 June 2026

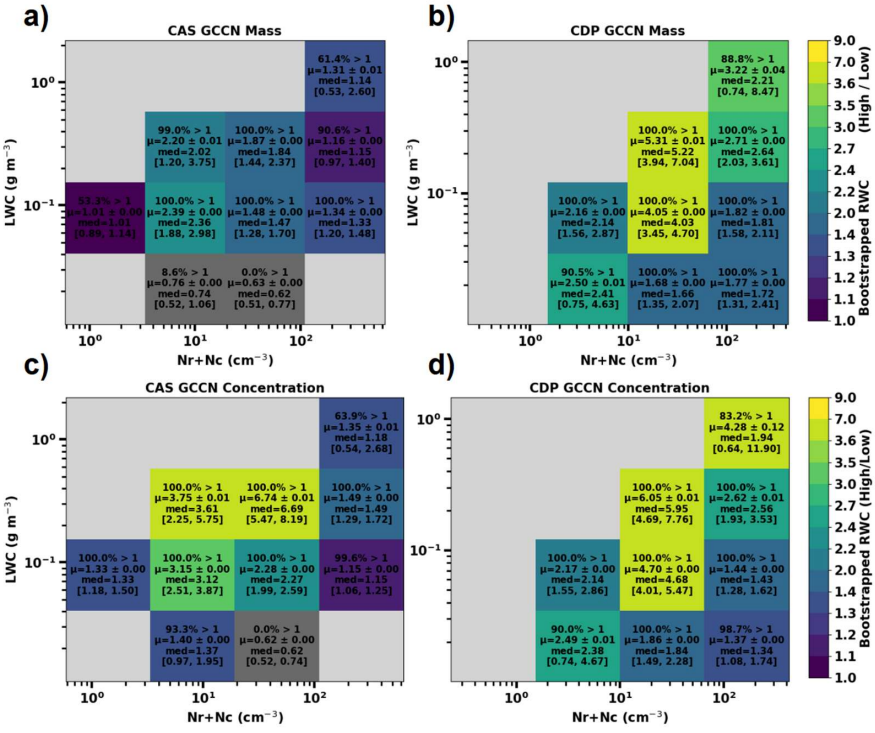

Figure 7 Observationally derived precipitation efficiency responses, defined as RWC/LWC, across bins (boxes) of LWC and N_d for cases with high versus low GCCN mass (top row) and high versus low GCCN concentration (bottom row), calculated separately for CAS (left column) and CDP (right column). Colors indicate the bootstrapped ratio of mean RWC/LWC in high GCCN cases relative to low GCCN cases within each bin (High/Low). Values greater than unity, which pertains to the colored boxes without gray shading, indicate a larger ratio under higher GCCN conditions. Text within each box shows the percentage of bootstrap realizations producing ratios greater than 1, the mean ratio +/- standard error of the mean, and the 90% confidence interval of the bootstrap distribution. Light gray bins indicate bins where fewer than 100 valid data points are available across the compared subsets and are excluded from analysis. Dark gray bins met the minimum sampling threshold but yielded bootstrap distributions whose mean ratio did not exceed 1, indicating no statistically robust enhancement of RWC/LWC under higher GCCN conditions in those bins.

Figure 7 shows that higher GCCN conditions are generally associated with enhanced RWC/LWC for the vast majority of the LWC-N_d bins. The observed differences in RWC/LWC also remained consistent across these thresholds, indicating that our results are robust with the 50% split. In all three split cases, the same pattern was observed; flights in the high GCCN category always exhibited larger RWC/LWC than flights in the low GCCN category across the same regions of LWC-N_d space. In all CDP bins with sufficient sampling, the ratio is >1 (Fig. 7b, d), while the CAS has 3 bins (two for GCCN mass and one for number concentration) where the mean ratio is <1 (Fig. 7a,c). For the CAS, all of these bins are located at very low LWC and moderate N_d. Overall, the majority of the bins with sufficient sampling for both instruments, contain data points where the ratio is exceeded by more than 90% of the data points in

https://doi.org/10.5194/egusphere-2026-3027
Preprint. Discussion started: 16 June 2026

that bin. This indicates that higher GCCN mass or concentration is typically associated with larger RWC/LWC values relative to lower GCCN conditions. This enhancement is especially robust (high confidence) in the central bins of the distribution, located at moderate levels of LWC and N_d, where the percentage of bootstrap realizations greater than 1 is near 100%.

Between the two instruments, the strongest enhancements are found with the CDP dataset, particularly for GCCN mass. In the CDP mass panel (7b) several bins exhibit mean values of 1.5-6. By contrast, the CAS mass panel (7a) does not show bins where mean RWC/LWC exceeds 2.4. The CDP mass analysis therefore shows stronger enhancement of RWC/LWC on average than the concentration analysis, while the CAS results show relatively stronger enhancement for GCCN concentration than for mass. The especially strong enhancements in the CDP mass panel support the model results from section 3.2 that GCCN mass may be a better predictor of precipitation response than GCCN concentration alone. The presence of sufficiently large particles versus the presence of more but smaller coarse mode appears to play a more important role in initiating collision-coalescence than number alone. Nevertheless, both probes suggest that rainwater contents are likely enhanced by a factor of 2 or more for GCCN mass in the upper half of the observed distribution compared with the lower half. This finding is broadly consistent with the modeling results (Fig. 5) that suggest precipitation accumulation may be approximately doubled for the upper half of the GCCN masses.

Furthermore, the highest ratios are not found uniformly across all bins. Instead, the largest RWC/LWC enhancements in Fig. 7 are in regions where Fig. 6 shows the highest mean RWC, corresponding to moderate-to-high LWC and relatively low-to-moderate Nd. For the CAS, bins with high LWC and high Nd yield lower ratios. Similarly, bins with lower LWC and low N_d show weaker enhancement, likely a result of insufficient condensate. The CDP shows a relatively similar pattern to the CAS in low LWC-N_d space; however, for both mass and concentration, the highest bin of LWC and N_d yields relatively high mean ratios (>3) than bins with the same N_d but lower LWC. This suggests that sufficiently high LWC might offset the suppressing effect of high by N_d promoting rapid droplet growth and increased collision-coalescence, thus allowing GCCN to enhance our metric of precipitation efficiency even in high N_d conditions.

4 Discussion

Together the ACTIVATE observational analysis in addition to results from the microphysics model provide a preponderance of evidence that GCCN are able to exert a significant influence on warm-rain formation. Both the in-situ measurements and model simulations show that increasing GCCN is associated with enhanced precipitation production, with GCCN mass exhibiting a stronger and more consistent relationship than number concentration. Due to the exponential nature of the GCCN size distribution for $D_{dry} > 2$ μm , GCCN number concentration tends to be dominated by salt particles with sizes close to the 2 μm threshold, but these particles are less effective at promoting precipitation than slightly particles with dry diameters in the range 4-10 μm (Barr and Wood 2026). This influence of GCCN appears to be captured well using the overall dry mass of salt particles, which suggests a possible way forward to parameterizing the GCCN effects on warm rain production in marine clouds. Our analyses also provide statistical observational evidence from a large number of clouds that LWC and N_d play an important role in staging the primary

https://doi.org/10.5194/egusphere-2026-3027
Preprint. Discussion started: 16 June 2026

conditions for precipitation formation, and that the presence of GCCN can impact how efficiently rain develops. The modeling provides additional support. Varying the submicron aerosol concentrations (N_a) and LWP have leading order influences on the production of warm rain (Terai et al. 2012; Pawlowska 2003, Van Zanten 2005; Wood 2005a, b; Mann 2014). Accumulated rainfall is greatest for low N_a conditions and weakest for low LWP conditions. Low N_a conditions promote collision-coalescence, while low LWP limits droplet growth and suppresses rainfall. Furthermore, RWC/LWC ratios were higher and more consistent for moderate LWC-N_d bins, thus showing strong agreement with model simulations. These comparisons are made within the same LWC-N_d regimes and therefore isolate the influence of GCCN. This demonstrates that enhanced precipitation efficiency is directly associated with the presence of GCCN rather than differences in cloud properties.

As in previous observational studies, our results demonstrate that, on average, higher wind speeds increase both the size and number of GCCN, though the impact is stronger for concentration. This positive relationship between increasing wind speed and GCCN production is consistent with other studies (Woodcock 1953; Monahan et al. 1986; Banner and Peregrine, 1993; Gemmrich and Farmer, 1999; Lewis and Schwartz 2004; Clarke et al. 2006; Colón-Robles et al., 2006; Jensen and Lee 2008; Jensen and Nugent 2017). In particular, Colón-Robles et al., 2006, which analyzed coarse-mode aerosols from a similar cloud probe (FSSP) to those used in this study, found a strong positive relationship between concentration and wind speed ($R = 0.87$, $R^2 = 0.76$) over a wind speed range of approximately 5-14 m s^{-1}, with a slope of 0.023 cm^{-3} (their Fig. 1a). Their wind speed range is very similar to ours, though they are looking at hydrated particles, whereas ours are dry. However, this is still comparable to our results, which show slopes of 0.033 +/- 0.015 μg $m^{-3}(m\ s^{-1})^{-1}$ and 0.029 +/- 0.022 μg $m^{-3}(m\ s^{-1})^{-1}$, for the CAS and CDP respectively (Table 1). Their correlation with wind speed for the FSSP is stronger than the CDP ($R^2 = 0.64$), but weaker than the CAS ($R^2 = 0.84$). The absolute concentrations reported by Colón-Robles et al. (2006) are generally lower than those observed here, with their Fig. 1a showing values ranging from about 0.05 to 0.3 cm^{-3} compared to about 0.1 to 0.6 cm^{-3} in this study (Fig. 4). Furthermore, their size distribution analysis (their Fig. 2) shows that stronger wind speeds increase particle concentrations across the coarse-mode spectrum, particularly for diameters larger than 10 μm (their Fig. 2a-b), with dry particle measurements from a Giant Nucleus Impactor (GNI) extending to 30-40 μm (their Fig. 2c). Our dry size distributions also follow exponential decay, with a tail extending to about 20-25 μm (Fig. 2), a slightly smaller range than in their GNI analysis. However, while both studies show the presence of large dry particles, the concentrations of these particles in Colón-Robles et al. (2006) decrease rapidly with increasing diameter and remain lower than ours beyond ~15 μm (their Fig. 2c). Our dry size distributions exhibit relatively higher concentrations across the coarse-mode tail, particularly in the 15-25 μm range. Though this study was based on 30-minute flight legs during the Rain in Shallow Cumulus over the Ocean (RICO) campaign (2004-2005) over the trade winds in the western Atlantic, the similarity in slope, correlation strength, and overlapping wind speed ranges indicates a consistent relationship between wind speed and coarse-mode aerosol concentration with this study. Although a positive relationship between wind speed and GCCN concentration is observed, the strength of this dependence is weaker than would be expected from sea spray aerosol flux parameterizations, which typically show a much stronger increase in particle production with wind speed (Woodcock 1953; Monahan et al., 1986; Lewis and Schwartz, 2004).

https://doi.org/10.5194/egusphere-2026-3027
Preprint. Discussion started: 16 June 2026

Furthermore, though our relationship between mass and wind speed is weaker than for concentration, it is still moderate and positive, consistent with other observational studies (Woodcock 1953; Liu et al., 2021). For example, Woodcock (1953) reports GCCN mass values of approximately ~8 μg m^{-3} at wind speeds of 5.5-7.9 m s^{-1} (their Fig. 2). In our study, the mean $M_{d>2}$ is 10.3 μg m^{-3} for the CAS and 12.2 μg m^{-3} for the CDP for a similar mean wind speed of 5.13 m s^{-1}, which falls within the Woodcock (1953) wind regime, further allowing us to directly compare between studies. Both our study and Woodcock (1953) show considerable amounts of scatter, reflected in the large spread of values within individual wind speed bins (Fig. 4) and the moderate coefficients of determination (R^2 = 0.61 and 0.54 for the CAS and CDP, respectively). Despite the agreement in magnitude, the relatively modest coefficients of determination and substantial scatter indicate that the dependence of GCCN mass on wind speed is weaker than would be expected from wind speed driven sea spray production alone. This highlights that variability in GCCN concentration and mass relationships cannot be explained by wind speed alone. Wind speed represents only one component of the processes controlling GCCN variability in the midlatitude marine environment.

Potential contributors to the remaining variability in GCCN not explained by wind speed are seasonal dependence, which may reflect changes in meteorological conditions such as rapidly changing wind regimes and sea surface temperature that can lead to changes in production rates or in the size of GCCN that are produced (Chen et al., 1973; Lewis and Schwartz 2004; Jaeglé et al., 2011; Painemal et al., 2021). There is an expected seasonal dependence on GCCN production because higher sea surface temperatures reduce water viscosity and impact bubble rise speeds and size distributions (Jaeglé et al., 2011). The ACTIVATE measurements used here span January-June, and so we examine the seasonal trend of GCCN mass, slope parameter, and concentration over the Western Atlantic (Fig. 8). These variables are shown as flight-leg mean values (section 2), organized chronologically by flight date, and grouped by month to highlight seasonal variability. Monthly summary statistics and inter-instrument agreement are also provided in Tables 2 and 3 to further quantify these trends.

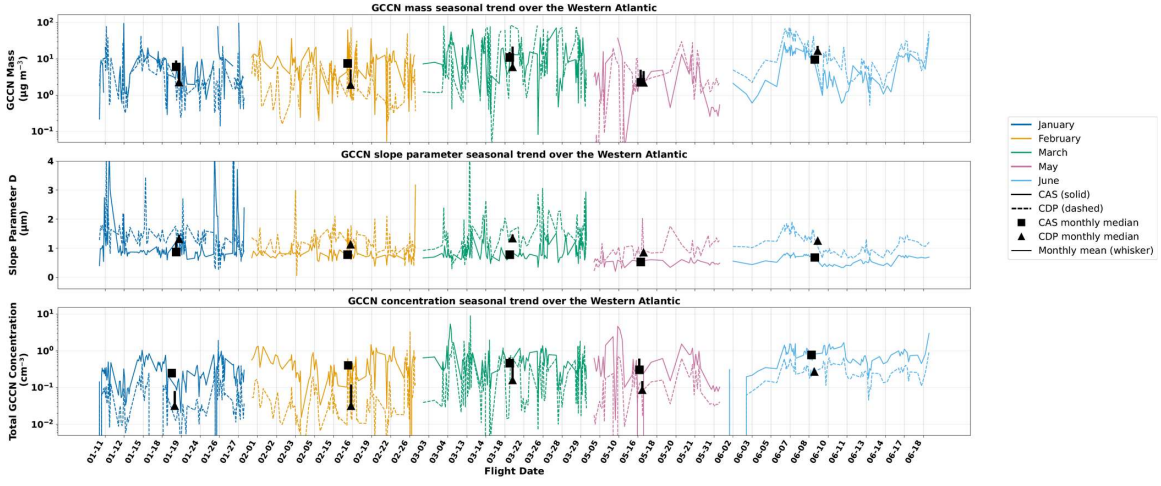

https://doi.org/10.5194/egusphere-2026-3027
Preprint. Discussion started: 16 June 2026

Figure 8 Monthly trends (January - June 2022) of GCCN mass $M_{d>2}$ (top), slope parameter $D_{e,dry}$ (middle), and total GCCN concentration $N_{d>2}$ (bottom). Values are shown as flight-leg means plotted by flight date and grouped by month. Solid lines (and black squares for monthly medians) represent measurements from the CAS, while dashed lines (and black triangles) represent measurements from the CDP. Whiskers on the black median symbols show the corresponding monthly means.

Monthly Correlations between CAS and CDP (r(R²))

Month	Mass (µg m^{-3})	Slope Parameter D (µm)	N_d (cm^{-3})
January	0.69 (0.48)	0.77 (0.59)	0.75 (0.57)
February	0.18 (0.033)	0.61 (0.37)	0.33 (0.11)
March	-0.26 (0.065)	0.089 (0.008)	0.026 (0.001)
May	0.54 (0.29)	-0.66 (0.43)	0.58 (0.34)
June	0.90 (0.81)	0.91 (0.83)	0.98 (0.97)
All months	**0.56 (0.31)**	**0.84 (0.70)**	**0.91 (0.83)**

Table 2 Monthly correlations between the CAS and the CDP across all months, as well as, within each month. GCCN mass $M_{d>2}$, slope parameter $D_{e,dry}$, and concentration $N_{d>2}$ shown as Pearson correlation coefficients r with corresponding coefficients of determination R^2 in parentheses. The full trends between the two instruments across all months are lowest and relatively weak for mass (R^2 =0.3) and highest for the slope parameter (R^2 =0.7) and number concentration (R^2 =0.8). For all three variables, intra-month CAS and the CDP estimates are mostly positively correlated, and are highest during the most in the month of June. The weaker correlation between the two instruments for GCCN mass measurements likely reflects a greater sensitivity of mass to more poorly sampled larger particles, which are less numerous and more variable in space and time, leading to increased measurement differences between instruments.

https://doi.org/10.5194/egusphere-2026-3027
Preprint. Discussion started: 16 June 2026

Monthly Summary Statistics (mean(median))

Month	CAS N_d (cm^{-3})	CDP N_d (cm^{-3})	CAS Slope Parameter D (μm)	CDP Slope Parameter D (μm)	CAS Mass (μg m^{-3})	CDP Mass (μg m^{-3})
January	0.31 (0.25)	0.08 (0.032)	1.2 (0.87)	1.4 (1.3)	9 (6)	5.6 (2.3)
February	0.47 (0.4)	0.12 (0.032)	0.82 (0.77)	1.2 (1.1)	9 (7.5)	5.1 (1.9)
March	0.65 (0.46)	0.47 (0.16)	0.91 (0.78)	1.5 (1.3)	15 (11)	21 (6)
May	0.62 (0.31)	0.15 (0.087)	0.53 (0.53)	0.9 (0.86)	5 (2.3)	4.6 (2.2)
June	0.79 (0.78)	0.29 (0.27)	0.63 (0.68)	1.2 (1.3)	9.7 (9.6)	23 (17)

Table 3 Monthly summary statistics for GCCN mass, slope parameter D, and concentration (N_d) measured by the CAS and CDP. Values are reported as monthly means, with corresponding medians in parentheses. Across all months, the CAS exhibits higher mean concentration, while the CDP generally shows larger slope parameters, indicating a greater relative contribution from larger particles. For January, February, and May, the CAS shows higher mass measurements, but the CDP records higher mass in March and June. No clear or consistent seasonal trend is observed across the sampled months.

In general, months with higher GCCN mass are associated with larger slope parameters (Table 3), indicating a shift toward relatively larger particles. However, GCCN concentration does not exhibit a consistent relationship with slope parameter as shown by the lack of a clear connection between monthly concentration and slope values (Table 3). Agreement between the CAS and CDP varies by variable and by month (Table 2). Across all months, correlations are strongest for concentration (R^2 = 0.83) and slope parameter (R^2 = 0.70), while substantially weaker for mass (R^2 = 0.31). However, this agreement is not uniform across individual months for any of the variables. For example, correlations are very weak in March for mass (R^2 = 0.065), slope parameter (R^2 = 0.008), and concentration (R^2 = 0.001), while much stronger in June (R^2 = 0.805, 0.832, and 0.969, respectively). These results indicate that while the two instruments capture similar overall trends, their agreement depends on both the variable considered and the temporal scale of analysis. For most months, the CAS exhibits a higher monthly median for mass and concentration, and a lower monthly median for slope compared to the CDP (Table 3). Across January through June 2022, there is no clear seasonal trend in GCCN mass, concentration, or slope parameter, as monthly means and medians do not show a consistent increase or decrease over time (Table 3). Instead, values fluctuate between months, including peaks and dips across individual flights within the same month (Fig. 8). GCCN properties across this time period appear to be driven more by individual flight conditions than by a coherent seasonal cycle, though this could be due to the conditions that were selectively targeted with each flight. The absence of a clear seasonal trend suggests that variations in GCCN mass, size, and concentration are not largely driven by large-scale seasonal changes.

However, to further investigate potential drivers of this variability, we also examined the seasonal behavior of wind speed, which is a primary control on sea-spray aerosol production. We show the seasonal evolution of GCCN mass and mean wind speed across the Western Atlantic (Fig. 9). This analysis focuses only on mass, as we found it to be

https://doi.org/10.5194/egusphere-2026-3027
Preprint. Discussion started: 16 June 2026

749 more influential in enhancing precipitation formation. As in Fig. 8, variables are shown as flight-leg means organized
750 chronologically by flight date and grouped by month to highlight seasonal variability.

751

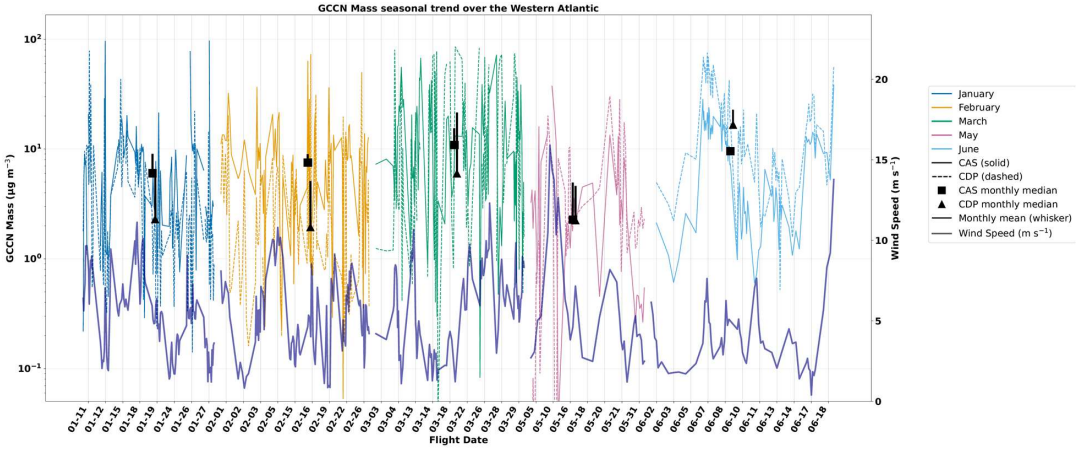

752

753 Figure 9 Monthly trends (January - June 2022) of mass are shown as flight leg means plotted by date and grouped by
754 month. Solid and dashed lines represent measurements from the CAS and CDP, respectively. Black squares (CAS)
755 and triangles (CDP) indicate monthly medians, with whiskers showing corresponding monthly means. The purple
756 line represents the mean flight leg wind speed (section 3.1).

757

758 Wind speed exhibits substantial variability between individual flight legs but does not show a systematic increase or
759 decrease from January through early June (Fig. 9). While a modest increase in both wind speed and GCCN mass is
760 observed toward the final flight dates in late June, this is not sustained throughout all months. For example, the short
761 periods of elevated mass for particular flights (e.g. March 13 and March 14) occurs without a corresponding substantial
762 increase in wind speed. Short-term decreases in both variables, such as those observed in early June, suggest some co-
763 variability, but this relationship is not consistent temporally. These results are consistent with the binned analysis
764 presented in section 3.1, where GCCN mass showed only a moderate dependence on wind speed. The wind speeds
765 recorded in ACTIVATE are relatively low; (< 16 m s^{-1}). It is possible that this relationship between mass and wind
766 speed might be stronger, given more extreme wind speeds. Overall, these results indicate that while wind speed likely
767 contributes to GCCN production on shorter timescales, it does not appear to be the dominant driver of changes in
768 GCCN mass.

769 The potential influence of sea surface temperature (SST) was not explicitly tested in this study. A more targeted
770 analysis using SST measurements, after accounting for the dependence of GCCN on wind speed, would help determine
771 whether SST explains additional variability in GCCN production. Despite the consistency of the results presented

https://doi.org/10.5194/egusphere-2026-3027
Preprint. Discussion started: 16 June 2026

here, several limitations of the analysis should be considered. First, while the ACTIVATE campaign contains an unprecedented amount of data due to its numerous flights, the aircraft did not contain a radar, which limits our ability to directly measure precipitation. Instead, we rely on in-situ measurements to derive rainwater content, which does not capture the precipitation falling out of the clouds and reaching the ground. Additionally, the relatively short duration of individual flight legs limits the sampled air volume, ~6×10^{-3} m³ for the CAS and ~7.7×10^{-3} m³, thus the need to bin flight legs for wind speed analysis. While counting uncertainties in total concentration are small (~0.01 cm^{-3}) and much smaller than the observed leg-to-leg variability, uncertainties in mass are slightly larger because mass is strongly influenced by the largest and least frequent particles. As reflected in Eq. (7), the mass uncertainty scales with D_i^6, making it particularly sensitive to incomplete sampling of the larger size range. As a result, individual flight legs may under or over represent large particles, leading to increased variability in mass estimates. Grouping flight legs into wind speed bins increases the effective sample volume and reduces this sampling noise.

As for the modeling setup, we must address the immaturity of our implementation of turbulence. We naively assumed that the collision efficiency is unaffected by changes in the geometric collision rates, but the total effect of how turbulence should change the collision rates of cloud droplets is considered an unsolved problem due to the extremely high computational cost required to compute such rates. In this study, we found that GCCN generally have a higher potential impact on precipitation than turbulence in each case (Fig. 5). Should any future increases in collision efficiency caused by turbulence be found to occur, it could ultimately change this finding. Regardless, we are much more confident in the robustness of the sensitivity of each non-turbulent case to GCCN.

Possible future work could build on this analysis by incorporating additional years of ACTIVATE observations, including data from 2020 and 2021, to better assess interannual variability. Furthermore, the use of instruments specifically designed to measure giant nuclei, such as a giant nucleus impactor, would provide improved characterization of the largest particles that dominate mass and are most relevant for collision-coalescence processes. These improvements would help further constrain the role of GCCN in precipitation formation and refine their representation in both observational and modeling frameworks. A step forward in this direction is demonstrated by some studies using cloud water samples to infer the amount of sea salt in clouds based on the mass concentration of its dominant species, sodium and chloride (Dadashazar et al., 2017; MacDonald et al., 2020; Gonzalez et al., 2022; Zeider et al., 2025; Ajayi et al., 2026).

5 Concluding Remarks

This study combined in-situ aircraft observations from the ACTIVATE campaign with super-droplet simulations to investigate the role of GCCN in warm-rain formation in marine low clouds over the western North Atlantic. Both observations and model simulations consistently indicate that increasing GCCN abundance enhances warm-rain formation, particularly in clouds with sufficient LWC and moderate N_d. While both GCCN concentration and mass increase with wind speed, the observed dependence is weaker than would be expected from sea-spray aerosol flux parameterizations, indicating that additional environmental factors contribute to GCCN variability in the marine atmosphere.

https://doi.org/10.5194/egusphere-2026-3027
Preprint. Discussion started: 16 June 2026

Together, the observational and modeling results provide evidence that GCCN influence precipitation development through enhanced collision-coalescence. GCCN mass was found to be a better predictor of precipitation enhancement than number concentration alone. Furthermore, our results are broadly consistent with previous studies that have identified positive relationships between wind speed and coarse-mode sea-salt aerosol production. However, the variability in our wind speed results demonstrates that wind speed alone is not enough to explain GCCN variability in mass and number concentration. Additional factors, including meteorological conditions, may contribute to the observed scatter.

Several limitations should be considered when interpreting these results. The ACTIVATE aircraft observations do not directly measure surface precipitation and rely instead on in-situ cloud and rainwater measurements. Additionally, estimates of GCCN mass remain sensitive to sampling uncertainties associated with the largest and least frequent particles. The representation of turbulence within the microphysical model also introduces uncertainty in the simulated precipitation response. Despite these limitations, the consistency between the observational and modeling analyses provides strong evidence that GCCN can substantially influence warm-rain formation in marine low clouds.

Overall, these findings improve our understanding of aerosol-cloud-precipitation interactions by demonstrating that coarse-mode sea spray aerosols can enhance precipitation efficiency even at relatively low concentrations. The stronger relationship between precipitation and GCCN mass than number concentration suggests that mass-based metrics may provide a useful framework for representing GCCN effects in future observational and modeling studies. Further analyses incorporating additional years of observations and targeted measurements of coarse mode seas salt particles would help better constrain the role of GCCN in marine clouds and their representation in microphysics models.

Code availability

The code used for data processing, analysis, and figure generation in this study is publicly available on GitHub. Scripts related to the CAS instrument are available at https://github.com/katherineemifsud/ACTIVATE-2024-2025/tree/master/CAS and scripts related to the CDP instrument are available at: https://github.com/katherineemifsud/ACTIVATE-2024-2025/tree/master/CDP. These repositories include routines for observational size distribution processing, statistical analysis, model comparison, and rainwater content analysis.

Data Availability

Data from the ACTIVATE campaign are publicly available through the NASA Atmospheric Science Data Center (ASDC) at https://doi.org/10.5067/SUBORBITAL/ACTIVATE/DATA001 and were accessed through the Sub-Orbital Order Tool (SOOT) at https://asdc.larc.nasa.gov/soot/browse/ACTIVATE/2022. The datasets are organized by year, aircraft platform, and instrument, with variables provided within each instrument category.

Author Contributions

KM and RW conceived the study. JB performed the model experiments. KM conducted the analysis and prepared the manuscript with contributions from co-authors.

https://doi.org/10.5194/egusphere-2026-3027
Preprint. Discussion started: 16 June 2026

Competing Interests

Disclaimer

Acknowledgments

The authors thank the science teams of NASA ACTIVATE for providing the datasets used in this study.

Financial Support

This research has been supported by the award NASA EVS-3 ACTIVATE (award 80NSSC23K0906) and the University of Washington Marine Cloud Brightening program which is funded by the generous support of a consortium of individual and foundation donors.

References

Ackerman, A. S., Kirkpatrick, M. P., Stevens, D. E., and Toon, O. B.: The impact of humidity above stratiform clouds on indirect aerosol climate forcing, *Nature*, 432, 1014–1017, doi:10.1038/nature03174, 2004.

Ajayi, T., Betito, G., Corral, A. F., Crosbie, E. C., Edwards, E.-L., Hilario, M. R. A., Shook, M. A., Winstead, E. L., Zeider, K., Ziemba, L. D., and Sorooshian, A.: Characteristics of Northwest Atlantic Cloud Water: PMF Applied to ACTIVATE's Cloud Water Data Set, ACS Earth Space Chem., doi:10.1021/acsearthspacechem.6c00028, 2026.

Albrecht, B. A.: Aerosols, cloud microphysics, and fractional cloudiness, *Science*, 245, 1227–1230, doi:10.1126/science.245.4923.1227, 1989.

Albrecht, B. A., Fairall, C. W., Thomson, D. W., White, A. B., Snider, J. B., and Schubert, W. H.: Surface-based remote sensing of the observed and the adiabatic liquid water content of stratocumulus clouds, *Geophys. Res. Lett.*, 17, 89–92, doi:10.1029/GL017i001p00089, 1990.

Banner, M. L. and Peregrine, D. H.: Wave breaking in deep water, *Annu. Rev. Fluid Mech.*, 25, 373–397, doi:10.1146/annurev.fl.25.010193.002105, 1993.

Barr, J.: Stochastic collection model for ACTIVATE, unpublished manuscript, 2025.

Baumgardner, D., Jonsson, H., Dawson, W., O'Connor, D., and Newton, R.: The cloud, aerosol and precipitation spectrometer: a new instrument for cloud investigations, *Atmos. Res.*, 59–60, 251–264, doi:10.1016/S0169-8095(01)00119-3, 2001.

Baumgardner, D., Abel, S. J., Axisa, D., Cotton, R., Crosier, J., Field, P., Gurganus, C., Heymsfield, A., Korolev, A., Krämer, M., Lawson, P., McFarquhar, G., Ulanowski, Z., and Um, J.: Cloud ice properties: In situ measurement challenges, in: *Ice Formation and Evolution in Clouds and Precipitation: Measurement and Modeling Challenges*, Meteor. Monogr., 58, 9.1–9.23, Amer. Meteor. Soc., doi:10.1175/AMSMONOGRAPHS-D-16-0011.1, 2017.

Beard, K. V. and Ochs, H. T.: Warm-rain initiation: an overview of microphysical mechanisms, *J. Appl. Meteorol.*, 32, 608–625, doi:10.1175/1520-0450(1993)032<0608:WRIAOO>2.0.CO;2, 1993.

https://doi.org/10.5194/egusphere-2026-3027
Preprint. Discussion started: 16 June 2026

Bellouin, N., Quaas, J., Gryspeerdt, E., Kinne, S., Stier, P., Watson-Parris, D., Boucher, O., et al.: Bounding global aerosol radiative forcing of climate change, *Rev. Geophys.*, 58, e2019RG000660, doi:10.1029/2019RG000660, 2020.

Berry, E. X.: Cloud droplet growth by collection, *J. Atmos. Sci.*, 24, 688–701, doi:10.1175/1520-0469(1967)024<0688:CDGBC>2.0.CO;2, 1967.

Berry, E. X. and Reinhardt, R. L.: An analysis of cloud drop growth by collection: Part I. Double distributions, *J. Atmos. Sci.*, 31, 1814–1824, doi:10.1175/1520-0469(1974)031<1814:AAOCDG>2.0.CO;2, 1974.

Chen, T., Zhang, Y., and Rossow, W. B.: Sensitivity of atmospheric radiative heating rate profiles to variations of cloud layer overlap, *J. Climate*, 13, 2941–2959, doi:10.1175/1520-0442(2000)013<2941:SOARHR>2.0.CO;2, 2000.

Chen, Y. C., Christensen, M. W., Xue, L., Sorooshian, A., Stephens, G. L., Rasmussen, R. M., and Seinfeld, J. H.: Occurrence of lower cloud albedo in ship tracks, *Atmos. Chem. Phys.*, 12, 8223–8235, doi:10.5194/acp-12-8223-2012, 2012.

Clarke, A. D., Owens, S. R., and Zhou, J.: An ultrafine sea-salt flux from breaking waves: Implications for cloud condensation nuclei in the remote marine atmosphere, *J. Geophys. Res.*, 111, D06202, doi:10.1029/2005JD006565, 2006.

Colón-Robles, M., Rauber, R. M., and Jensen, J. B.: Influence of low-level wind speed on droplet spectra near cloud base in trade wind cumulus, *Geophys. Res. Lett.*, 33, L20814, doi:10.1029/2006GL027487, 2006.

Cooper, W. A., Lasher-Trapp, S. G., and Blyth, A. M.: The influence of entrainment and mixing on rain formation in warm cumulus clouds, *J. Atmos. Sci.*, 70, 1727–1743, doi:10.1175/JAS-D-12-0128.1, 2013.

Dadashazar, H., Wang, Z., Crosbie, E., Brunke, M., Zeng, X., Jonsson, H., Woods, R. K., Flagan, R. C., Seinfeld, J. H., and Sorooshian, A.: Relationships between giant sea salt particles and clouds inferred from aircraft physicochemical data, J. Geophys. Res. Atmos., 122, 3421–3434, doi:10.1002/2016JD026019, 2017.

Dadashazar, H., Corral, A. F., Crosbie, E., Dmitrovic, S., Kirschler, S., McCauley, K., Moore, R., et al.: Organic enrichment in droplet residual particles relative to out of cloud over the northwestern Atlantic: Analysis of airborne ACTIVATE data, *Atmos. Chem. Phys.*, 22, 13897–13913, doi:10.5194/acp-22-13897-2022, 2022.

Davis, J. T., and Kreidenweis, S. M.: Large particle characteristics over the Southern Ocean during ACE 1, unpublished report, Colorado State University, Fort Collins, CO, USA, 1999.

Diskin, G. S., Podolske, J. R., Sachse, G. W., and Slate, T. A.: Open-path airborne tunable diode laser hygrometer, Proc. SPIE, 4817, 196–204, doi:10.1117/12.453736, 2002.

Diskin, G.: DLH: Diode laser hygrometer measurements of H_2O(v), NASA Langley Research Center dataset, 2022.

Dziekan, P., Jensen, J. B., Grabowski, W. W., and Pawlowska, H.: Impact of giant sea salt aerosol particles on precipitation in marine cumuli and stratocumuli: Lagrangian cloud model simulations, *J. Atmos. Sci.*, 78, 2627–2643, doi:10.1175/JAS-D-21-0041.1, 2021.

Feingold, G., Cotton, W. R., Kreidenweis, S. M., and Davis, J. T.: The impact of giant cloud condensation nuclei on drizzle formation in stratocumulus: Implications for cloud radiative properties, *J. Atmos. Sci.*, 56, 4100–4117, doi:10.1175/1520-0469(1999)056<4100:TIOGCC>2.0.CO;2, 1999.

Flossmann, A. I., Hall, W. D., and Pruppacher, H. R.: A theoretical study of the wet removal of atmospheric pollutants. Part I: Redistribution of aerosol particles, *J. Atmos. Sci.*, 42, 583–606, doi:10.1175/1520-0469(1985)042<0583:ATSOTW>2.0.CO;2, 1985.

https://doi.org/10.5194/egusphere-2026-3027
Preprint. Discussion started: 16 June 2026

Gemmrich, J. R. and Farmer, D. M.: Observations of the scale and occurrence of breaking surface waves, *J. Phys. Oceanogr.*, 29, 2595–2606, doi:10.1175/1520-0485(1999)029<2595:OOTSAO>2.0.CO;2, 1999.

Glienke, S., Kostinski, A., Fugal, J. P., Shaw, R. A., Borrmann, S., and Stith, J.: Cloud droplets to drizzle: Contribution of transition drops to microphysical and optical properties of marine stratocumulus clouds, *Geophys. Res. Lett.*, 44, 8002–8010, doi:10.1002/2017GL074430, 2017.

Gonzalez, M. E., Corral, A. F., Crosbie, E., Dadashazar, H., Diskin, G. S., Edwards, E.-L., Kirschler, S., Moore, R. H., Robinson, C. E., Schlosser, J. S., Shook, M., Stahl, C., Thornhill, K. L., Voigt, C., Winstead, E., Ziemba, L. D., and Sorooshian, A.: Relationships between supermicrometer particle concentrations and cloud water sea salt and dust concentrations: analysis of MONARC and ACTIVATE data, Environ. Sci.: Atmos., doi:10.1039/D2EA00049K, 2022.

Hartmann, D. L., Ockert-Bell, M. E., and Michelsen, M. L.: The effect of cloud type on Earth's energy balance: Global analysis, *J. Climate*, 5, 1281–1304, doi:10.1175/1520-0442(1992)005<1281:TEOCTO>2.0.CO;2, 1992.

Hartmann, D. L. and Short, D. A.: On the use of Earth radiation budget statistics for studies of clouds and climate, *J. Atmos. Sci.*, 37, 1233–1250, doi:10.1175/1520-0469(1980)037<1233:OTUOER>2.0.CO;2, 1980.

Heintzenberg, J., Covert, D. C., and van Dingenen, R.: Size distribution and chemical composition of marine aerosols: A compilation and review, *Tellus B*, 52, 1104–1122, doi:10.3402/tellusb.v52i4.17090, 2000.

Hocking, L. M.: The collision efficiency of small drops, *Q. J. Roy. Meteorol. Soc.*, 85, 44–50, doi:10.1002/qj.49708536305, 1959.

Jaeglé, L., Quinn, P. K., Bates, T. S., Alexander, B., and Lin, J.-T.: Global distribution of sea salt aerosols: New constraints from in situ and remote sensing observations, *Atmos. Chem. Phys.*, 11, 3137–3157, doi:10.5194/acp-11-3137-2011, 2011.

Jensen, J. B. and Lee, S.: Giant sea-salt aerosols and warm rain formation in marine stratocumulus, *J. Atmos. Sci.*, 65, 3678–3694, doi:10.1175/2008JAS2617.1, 2008.

Jensen, J. B. and Nugent, A. D.: Condensational growth of drops formed on giant sea-salt aerosol particles, *J. Atmos. Sci.*, 74, 679–697, doi:10.1175/JAS-D-15-0370.1, 2017.

Johnson, D. B.: The role of giant and ultragiant aerosol particles in warm rain initiation, *J. Atmos. Sci.*, 39, 448–460, doi:10.1175/1520-0469(1982)039<0448:TROGAU>2.0.CO;2, 1982.

Khairoutdinov, M. and Kogan, Y.: A new cloud physics parameterization in a large-eddy simulation model of marine stratocumulus, *Mon. Weather Rev.*, 128, 229–243, doi:10.1175/1520-0493(2000)128<0229:ANCPPI>2.0.CO;2, 2000.

Kirschler, S., Voigt, C., Anderson, B., Campos Braga, R., Chen, G., Corral, A. F., Crosbie, E., et al.: Seasonal updraft speeds change cloud droplet number concentrations in low-level clouds over the western North Atlantic, *Atmos. Chem. Phys.*, 22, 8299–8319, doi:10.5194/acp-22-8299-2022, 2022.

Kumar, S. and Ramkrishna, D.: On the solution of population balance equations by discretization—I. A fixed pivot technique, *Chem. Eng. Sci.*, 51, 1311–1332, doi:10.1016/0009-2509(96)88489-2, 1996.

Lance, S.: Coincidence errors in a cloud droplet probe (CDP) and a cloud and aerosol spectrometer (CAS), and the improved performance of a modified CDP, *J. Atmos. Ocean. Technol.*, 29, 1532–1541, doi:10.1175/JTECH-D-11-00208.1, 2012.

https://doi.org/10.5194/egusphere-2026-3027
Preprint. Discussion started: 16 June 2026

Lebo, Z. J. and Morrison, H.: A novel scheme for parameterizing aerosol processing in warm clouds, *J. Atmos. Sci.*, 70, 3576–3598, doi:10.1175/JAS-D-13-045.1, 2013.

L'Ecuyer, T. S., Berg, W., Haynes, J., Lebsock, M., and Takemura, T.: Global observations of aerosol impacts on precipitation occurrence in warm maritime clouds, *J. Geophys. Res.*, 114, D09211, doi:10.1029/2008JD011273, 2009.

L'Ecuyer, T. S., Hang, Y., Matus, A. V., and Wang, Z.: Reassessing the effect of cloud type on Earth's energy balance in the age of active spaceborne observations. Part I: Top of atmosphere and surface, *J. Climate*, 32, 6947–6965, doi:10.1175/JCLI-D-18-0753.1, 2019.

Lewis, E. R. and Schwartz, S. E.: Methods of determining size-dependent sea salt aerosol production fluxes, in: *Sea Salt Aerosol Production: Mechanisms, Methods, Measurements and Models*, AGU, 101–118, doi:10.1002/9781118666050.ch3, 2004.

Lewis, E. R. and Schwartz, S. E.: Sea salt aerosol production: mechanisms, methods, measurements, and models – a critical review, NOAA Tech. Rep., NOAA, available at: https://repository.library.noaa.gov/view/noaa/48979, 2004.

Li, J., Carlson, B. E., Yung, Y. L., Lv, D., Hansen, J., Penner, J. E., Liao, H., et al.: Scattering and absorbing aerosols in the climate system, *Nat. Rev. Earth Environ.*, 3, 363–379, doi:10.1038/s43017-022-00296-7, 2022.

Lowenstein, J. H., Blyth, A. M., and Lawson, R. P.: Early evolution of the largest-sized droplets in maritime cumulus clouds, *Q. J. Roy. Meteorol. Soc.*, 136, 708–717, doi:10.1002/qj.597, 2010.

Ludlam, F. H.: The production of showers by the coalescence of cloud droplets, *Q. J. Roy. Meteorol. Soc.*, 77, 402–417, doi:10.1002/qj.49707733306, 1951.

MacDonald, A. B., Hossein Mardi, A., Dadashazar, H., Azadi Aghdam, M., Crosbie, E., Jonsson, H. H., Flagan, R. C., Seinfeld, J. H., and Sorooshian, A.: On the relationship between cloud water composition and cloud droplet number concentration, Atmos. Chem. Phys., 20, 7645–7665, doi:10.5194/acp-20-7645-2020, 2020.

Mann, J. A. L., Chiu, J. C., Hogan, R. J., O'Connor, E. J., L'Ecuyer, T. S., Stein, T. H. M., and Jefferson, A.: Aerosol impacts on drizzle properties in warm clouds from ARM Mobile Facility deployments, *J. Geophys. Res.*, 119, 2013JD021339, doi:10.1002/2013JD021339, 2014.

Monahan, E. C., Fairall, C. W., Davidson, K. L., and Boyle, P. J.: Observed inter-relations between 10 m winds, ocean whitecaps and marine aerosols, *Q. J. Roy. Meteorol. Soc.*, 109, 379–392, doi:10.1002/qj.49710946010, 1983.

Mülmenstädt, J. and Feingold, G.: The radiative forcing of aerosol–cloud interactions in liquid clouds: Wrestling and embracing uncertainty, *Curr. Clim. Change Rep.*, 4, 23–40, doi:10.1007/s40641-018-0089-y, 2018.

Painemal, D., Corral, A. F., Sorooshian, A., Brunke, M. A., Chellappan, S., Gorooh, V. A., Ham, S.-H., O'Neill, L., Smith Jr., W. L., and coauthors: An overview of atmospheric features over the western North Atlantic Ocean and North American east coast-Part 2: Circulation, boundary layer, and clouds, J. Geophys. Res. Atmos., 126, https://doi.org/10.1029/2020JD033423, 2021.

Pawlowska, H.: An observational study of drizzle formation in stratocumulus clouds for general circulation model parameterizations, *J. Geophys. Res.*, 108, D15, doi:10.1029/2002JD002679, 2003.

Peña Díaz, A., Gryning, S.-E., and Hasager, C. B.: Measurements and modelling of the wind speed profile in the marine atmospheric boundary layer, *Bound.-Lay. Meteorol.*, 129, 479–495, doi:10.1007/s10546-008-9323-9, 2008.

Petters, M. D. and Kreidenweis, S. M.: A single parameter representation of hygroscopic growth and cloud condensation nucleus activity, *Atmos. Chem. Phys.*, 7, 1961–1971, doi:10.5194/acp-7-1961-2007, 2007.

https://doi.org/10.5194/egusphere-2026-3027
Preprint. Discussion started: 16 June 2026

Posselt, R. and Lohmann, U.: Influence of giant CCN on warm rain processes in the ECHAM5 GCM, *Atmos. Chem. Phys.*, 8, 3769–3788, doi:10.5194/acp-8-3769-2008, 2008.

Rémillard, J., Kollias, P., Luke, E., and Wood, R.: Marine boundary layer cloud observations in the Azores, *J. Climate*, 25, 7381–7398, doi:10.1175/JCLI-D-11-00610.1, 2012.

Sanchez, K. J., Moore, R. H., Anderson, B. E., Crosbie, E. C., Ziemba, L. D., Shook, M. A., Thornhill, K. L., Winstead, E. L., and Sorooshian, A.: Multi-campaign ship and aircraft observations of marine cloud condensation nuclei and cloud droplet number concentrations, *Sci. Data*, 10, 498, doi:10.1038/s41597-023-02318-1, 2023.

Seinfeld, J. H. and Pandis, S. N.: *Atmospheric Chemistry and Physics: From Air Pollution to Climate Change*, 2nd edn., Wiley, Hoboken, NJ, 2006.

Seinfeld, J. H., Bretherton, C., Carslaw, K. S., Coe, H., DeMott, P. J., Dunlea, E. J., Feingold, G., et al.: Improving our fundamental understanding of the role of aerosol–cloud interactions in the climate system, *Proc. Natl. Acad. Sci. USA*, 113, 5781–5790, doi:10.1073/pnas.1514043113, 2016.

Shima, S., Kusano, K., Kawano, A., Sugiyama, T., and Kawahara, S.: The super-droplet method for the numerical simulation of clouds and precipitation, *Q. J. Roy. Meteorol. Soc.*, 135, 1307–1320, doi:10.1002/qj.441, 2009.

Shima, S.-I., Sato, Y., Hashimoto, A., and Misumi, R.: Predicting the morphology of ice particles in deep convection using the super-droplet method: development and evaluation of SCALE-SDM 0.2.5–2.2.0, -2.2.1, and -2.2.2, *Geosci. Model Dev.*, 13, 4107–4157, doi:10.5194/gmd-13-4107-2020, 2020.

Sorooshian, A., Alexandrov, M. D., Bell, A. D., Bennett, R., Betito, G., Burton, S. P., Buzanowicz, M. E., et al.: Spatially coordinated airborne data and complementary products for aerosol, gas, cloud, and meteorological studies: The NASA ACTIVATE dataset, *Earth Syst. Sci. Data*, 15, 3419–3472, doi:10.5194/essd-15-3419-2023, 2023.

Stephens, G. L. and Greenwald, T. J.: The Earth's radiation budget and its relation to atmospheric hydrology: 2. Observations of cloud effects, *J. Geophys. Res.*, 96, 15325–15340, doi:10.1029/91JD00972, 1991.

Stevens, B., Cotton, W. R., Feingold, G., and Moeng, C.-H.: Large-eddy simulations of strongly precipitating, shallow, stratocumulus-topped boundary layers, *J. Atmos. Sci.*, 55, 3616–3638, doi:10.1175/1520-0469(1998)055<3616:LESOSP>2.0.CO;2, 1998.

Stevens, B. and Feingold, G.: Untangling aerosol effects on clouds and precipitation in a buffered system, *Nature*, 461, 607–613, doi:10.1038/nature08281, 2009.

Stull, R. B.: *An Introduction to Boundary Layer Meteorology*, Kluwer Academic Publishers, Dordrecht, 1988.

Tang, I. N.: Chemical and size effects of hygroscopic aerosols on light scattering coefficients, *J. Geophys. Res.*, 101, 19245–19250, doi:10.1029/96JD03003, 1996.

Tang, I. N., Tridico, A. C., and Fung, K. H.: Thermodynamic and optical properties of sea salt aerosols, *J. Geophys. Res.*, 102, 23269–23275, doi:10.1029/97JD01806, 1997.

Terai, C. R., Wood, R., Leon, D. C., and Zuidema, P.: Does precipitation susceptibility vary with increasing cloud thickness in marine stratocumulus?, *Atmos. Chem. Phys.*, 12, 4567–4583, doi:10.5194/acp-12-4567-2012, 2012.

Thornhill, K. L.: In situ state and aircraft measurements from the NASA HU-25, ACTIVATE, NASA Langley Research Center.

Twomey, S.: The influence of pollution on the shortwave albedo of clouds, *J. Atmos. Sci.*, 34, 1149–1152, doi:10.1175/1520-0469(1977)034<1149:TIOPOT>2.0.CO;2, 1977.

https://doi.org/10.5194/egusphere-2026-3027
Preprint. Discussion started: 16 June 2026

1034 von Salzen, K., Akingunola, A., Cole, J. N. S., Digby, R. A. R., Doherty, S. J., Fraser-Leach, L., Gryspeerdt, E.,
1035 Sigmond, M., and Wood, R.: Reduced aerosol pollution diminished cloud reflectivity over the North Atlantic and
1036 Northeast Pacific, *Nat. Commun.*, 16, 9433, doi:10.1038/s41467-025-65127-x, 2025.

1037 Wang, H., Feingold, G., Wood, R., and Kazil, J.: Sensitivity of precipitation to aerosol perturbations in marine
1038 stratocumulus, *Geophys. Res. Lett.*, 44, 2017GL074430, doi:10.1002/2017GL074430, 2017.

1039 Wood, R.: Drizzle in stratiform boundary layer clouds. Part I: Vertical and horizontal structure, *J. Atmos. Sci.*, 62,
1040 3011–3033, doi:10.1175/JAS3529.1, 2005.

1041 Wood, R.: Stratocumulus clouds, *Mon. Weather Rev.*, 140, 2373–2423, doi:10.1175/MWR-D-11-00121.1, 2012.

1042 Wood, R. and Bretherton, C. S.: On the relationship between stratiform low cloud cover and lower-tropospheric
1043 stability, *J. Climate*, 19, 6425–6432, doi:10.1175/JCLI3988.1, 2006.

1044 Wood, R.: Cancellation of aerosol indirect effects in marine stratocumulus through cloud thinning, *J. Atmos. Sci.*,
1045 64, 2657–2669, doi:10.1175/JAS3942.1, 2007.

1046 Wood, R., Kubar, T. L., and Hartmann, D. L.: Understanding the importance of microphysics and macrophysics for
1047 warm rain in marine low clouds. Part II: Heuristic models of rain formation, *J. Atmos. Sci.*, 66, 2971–2989,
1048 doi:10.1175/2009JAS3072.1, 2009.

1049 Woodcock, A. H.: Salt nuclei in marine air as a function of altitude and wind force, *J. Atmos. Sci.*, 10, 362–371,
1050 doi:10.1175/1520-0469(1953)010<0362:SNIMAA>2.0.CO;2, 1953.

1051 Zeider, K., McCauley, K., Dmitrovic, S., Siu, L. W., Choi, Y., Crosbie, E. C., DiGangi, J. P., Diskin, G. S.,
1052 Kirschler, S., Nowak, J. B., Shook, M. A., Thornhill, K. L., Voigt, C., Winstead, E. L., Ziemba, L. D., Zuidema, P.,
1053 and Sorooshian, A.: Sensitivity of aerosol and cloud properties to coupling strength of marine boundary layer clouds
1054 over the northwest Atlantic, Atmos. Chem. Phys., 25, 2407–2422, doi:10.5194/acp-25-2407-2025, 2025.

1055 Zmijewski, P., Dziekan, P., and Pawlowska, H.: Modeling collision–coalescence in particle microphysics:
1056 Numerical convergence of mean and variance of precipitation in cloud simulations using the University of Warsaw
1057 Lagrangian Cloud Model (UWLCM) 2.1, *Geosci. Model Dev.*, 17, 759–780, doi:10.5194/gmd-17-759-2024, 2024.